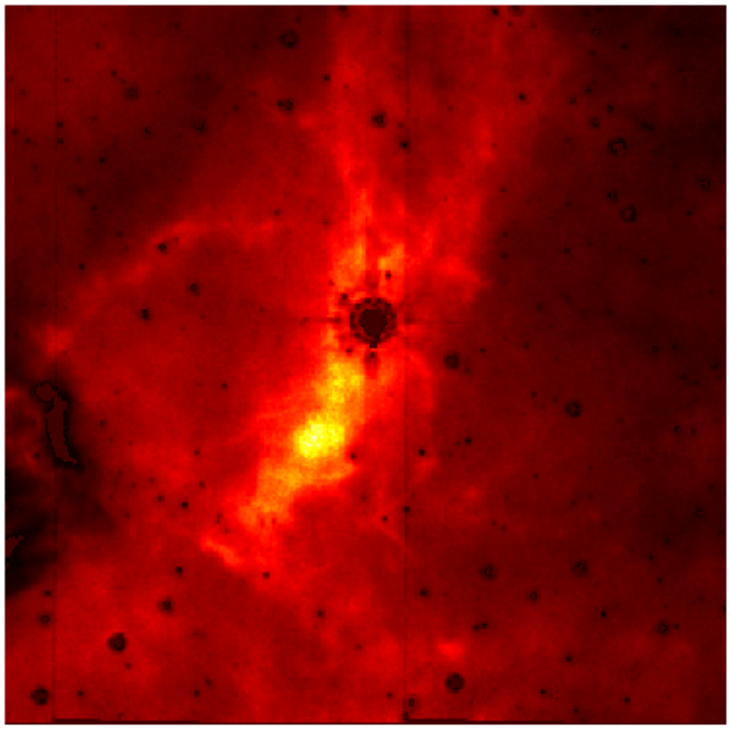

Massive Star Formation

Analysis of the kinematic and physical conditions of massive cores in the infrared dark cloud G28.23-0.19

Bachelor's thesis in Engineering Physics, SEEX15-21-83
Supervisors: Giuliana Cosentino, Rubén Fedriani and Prasanta Gorai
Examiners: Jonathan Tan and Eva Wirström

Johanna Brinkmalm
Karin Hult
Mattias Wiklund

Department of Space, Earth and Environment
CHALMERS UNIVERSITY OF TECHNOLOGY
Gothenburg, Sweden, 17 May 2021

Abstract

Massive stars play an important role in the Universe, affecting the evolution of galaxies and formation of planets. However, it is challenging to observe and investigate the initial stages of their formation. It is therefore of interest to study infrared dark clouds (IRDCs), where massive stars are believed to be born. In this thesis, the kinematic and physical conditions of the IRDC G28.23-0.19 was examined with purpose of analysing its potential to form massive stars. Using a mass surface density map, seven massive cores in the IRDC were identified. A multi-wavelength IR analysis were performed at the wavelengths 4.5, 8, 24 and 70 µm in order to estimate the relative evolutionary stages of the cores. The general lack of emission indicates that the cores likely are quiescent or in an early evolutionary stage. Thereafter, the kinematic structure of the cloud and its cores was examined by analysing the spectra for the $J = 1 \rightarrow 0$ rotational transition for ^{13}CO and C^{18}O, respectively. In general, the cloud seems to be moving with one velocity component at 80 km/s. Moreover, none of the line profiles showed broad wings, indicating an absence of outflow activity in the cloud and therefore possibly early evolutionary stages. Following this, the CO depletion factors for the cloud and its cores were estimated. The obtained values of 2.5−5.3 are lower than those generally found in massive starless cores. This could, contrary to above, potentially indicate a later evolutionary stage. Lastly, a virial analysis was performed. The virial parameters obtained for the cores (6.5−12) could potentially indicate a gravitationally unbound state, and that they might not be likely to undergo massive star formation. In summary, G28.23-0.19, in agreement with earlier studies, shows no clear indication of active formation of massive stars. However, further investigations are needed in order to draw more general conclusions.

Sammandrag

Massiva stjärnor spelar en viktig roll i universum och påverkar såväl utveckling av galaxer som formation av planeter. Det är emellertid svårt att studera och undersöka de första stadierna i deras utveckling, vilket motiverar studier av infraröda mörka moln (IRDCs), där massiva stjärnor troligen blir till. I det här arbetet undersöktes de kinematiska och fysiska egenskaperna hos IRDC G28.23-0.19 i syfte att analysera dess potential att bilda massiva stjärnor. Genom användning av en ytdensitetskarta kunde sju massiva kärnor identifieras. En IR-analys för våglängderna 4.5, 8, 24 och 70 µm utfördes sedan i syfte att uppskatta kärnornas relativa utvecklingsstadier. Avsaknaden av emission tyder på att kärnorna inte är aktiva, alternativt i ett tidigt utvecklingsstadium. Därefter undersöktes den kinematiska strukturen hos molnet genom analys av spektra för rotationsövergången $J = 1 \rightarrow 0$ för ^{13}CO respektive C^{18}O. I allmänhet uppvisade molnet en gemensam hastighetkomponent runt 80 km/s. Ingen av linjeprofilerna påvisade breda vingar, vilket tyder på avsaknad av utflöde och således potentiellt tidiga utvecklingsstadier. Efter detta uppskattades, för molnet och dess kärnor, andelen CO som bundit till stoftkorn. De erhållna värdena, 2.5−5.3, är något lägre jämfört de i massiva, stjärnlösa kärnor. Detta kan, i motsats till ovan, indikera ett senare utvecklingsstadium. Slutligen utfördes även en virialanalys. De virala parametrarna för kärnorna (6.5−12) kan indikera ett gravitationellt obundet system, och att det inte är troligt att kärnorna kommer att bilda massiva stjärnor. Sammanfattningsvis visar G28.23-0.19, i överensstämmelse med tidigare studier, inga tydliga tecken på aktiv stjärnformation. Ytterligare studier krävs emellertid för att kunna erhålla mer allmänna slutsatser.

Keywords: Massive stars, massive cores, infrared dark clouds, mass surface density, emission spectrum, column density, depletion, virial analysis.

Cover: Mass surface density map of the IRDC G28.23-0.19.

Acknowledgements

We would like to thank our supervisors Giuliana Cosentino, Rubén Fedriani and Prasanta Gorai for their tireless commitment and enormous support, as well as for their rewarding meetings and lectures, throughout the whole process. We would also like to thank our examiners Jonathan Tan and Eva Wirström, who enabled us to work on this interesting project.

Johanna Brinkmalm, Karin Hult, Mattias Wiklund
Gothenburg, 17 May 2021

Contents

1

Introduction

Stars with a mass higher than eight times that of the Sun are known as massive stars. These objects play an important role in the synthesis and dispersion of heavy elements and inject vast amounts of energy in the interstellar medium (ISM), ultimately regulating the evolution of galaxies (Tan et al. 2014). Even though massive stars play a crucial role in the Universe, it is not yet known how they form. It is unknown how the large amount of material necessary is gathered in the relatively small time scales over which massive stars evolve. Low mass star formation is relatively well understood, but this process cannot produce stars with a mass higher than 20 $M_{\odot}$ (Shu 1977).

1.1 The problem of massive star formation

Indeed, the theory of low mass star formation cannot be adapted to that of massive star formation. Low mass star formation begins when a dense cloud collapses under its own gravity, which will occur when the mass exceeds a critical threshold known as Jeans mass (Jeans 1928). The initially optically thin gas then becomes compressed and heated, dissipating the heat through radiative transfer. The gas temperature remains constant, but the compression of the gas causes the density to increase which enables smaller cloud portions to collapse, leading to fragmentation. This results in the formation of several low mass stars instead of one massive star and is known as the fragmentation problem. Another reason that prevents massive stars from forming this way is the gas becoming optically thick as the cloud collapses, hence the heat is obstructed from being radiated away. The action of the radiation pressure against gravity stops the accretion of the cloud since radiative losses are not efficient anymore. To fully understand massive star formation, new theories must be tested.

There are currently two main theories that have been proposed to explain how massive stars can accrete material. These differ primarily in how and when the material is gathered. The first is known as *core accretion* and can be seen as a scaled-up version of low mass star formation. Here the initial conditions are self-gravitating (Krumholz & Bonnell 2009; McKee & Tan 2003). In a pre-stellar stage due to the overlying pressure of the surrounding, fragmenting clump environment, the mass is gathered. Turbulence supports the core against gravity, allowing more material to be accreted than in the low-mass case. The centrally concentrated cores then undergo gravitational collapse via a central disk to form a star. Jets and ouflows are launched by the massive protostar, carrying out enormous amounts of energy that shape the parental cloud (Bally 2016).

The second theory is called *competitive accretion*. Here the mass is gathered during the star formation process itself (Krumholz & Bonnell 2009). It occurs more chaotically as the material is drawn, without being in a massive, coherent core, from a wider region in the surrounding clump environment (Tan et al. 2014). The competitive accretion scenario naturally explains how most stars are formed in clusters, rather than in isolation.

From an observational point of view, it is extremely challenging to investigate the initial

stages of massive star formation. Massive stars are indeed located very far away (in the order of a few kiloparsecs) and therefore need to be observed with the most powerful telescopes (Sanhueza et al. 2013). Furthermore, they are often located in crowded environments, making it very difficult to isolate one specific star from the contributions of different nearby forming objects. Additionally, the massive stars in the early stages are often embedded in a thick and opaque layer of gas and dust that prevents the observation of the massive star formation process (Sanhueza et al. 2013). A way to avoid this problem is to study the regions believed to be the birthplace of massive stars, which is why regions known as infrared dark clouds (IRDCs) are of great interest.

1.2 Infrared dark clouds: birthplaces of massive stars

IRDCs are the densest parts of large structures known as giant molecular clouds (GMCs) and were discovered by large scale observations of IR wavelengths performed between 1995 and 1998 (Egan et al. 1998; Perault et al. 1996). These clouds are detected between 1−8 kpc from the Sun across the Galactic plane (Carey et al. 1998). IRDCs absorb Galactic background mid-IR emission and are seen as dark areas in the Galaxy when observed, hence "dark clouds" (Egan et al. 1998). To observe them, radio telescopes are needed since IRDCs emit radiation at longer wavelengths such as far-IR, millimetre and submillimetre.

IRDCs are generally characterised by their high mass (10^3-10^5 $M_\odot$) (Sanhueza et al. 2013) and low temperature, usually below 25 K (Chira et al. 2013; Pillai et al. 2006). Typical column densities of IRDCs are around 10^{23} cm^{-2} (Sanhueza et al. 2013), similar to those regions known to be forming massive stars. These objects also host cold IR-dark clumps known as cold cores, considered the first stage of massive star formation (Rathborne et al. 2007). Consequently, it is clear that IRDCs has the conditions required for massive star formation and by studying them, it is possible to identify the initial physical and chemical conditions necessary to form massive stars.

To study these properties of molecular clouds in greater depth, several tracers can be studied. In this context, tracers can be seen as different types of molecular species, or infrared radiation, that indicate certain properties for the cloud. For example, observations of the rotational transitions of several molecular species enables detailed study of physical and chemical properties. A common tracer of molecular gas is the CO(1−0) transition at 2.6 mm (Tielens 2010). Although molecular clouds consist of several molecular species, H_2 is the most abundant molecule. CO is the second most abundant, with a H_2/CO ratio around 10^4-10^5. However, in the ISM, H_2 is rarely excited above its ground state due to the large spacing of its rotational levels (Heyer & Dame 2015) and is therefore ill suited for observations in IRDCs. Other molecular species that can be observed are for example N_2H^+, known to be a selective tracer of quiescent gas, particularly suited for the study of kinematics and structure in cold star-forming cores (Vasyunina et al. 2011). Another molecular species that could be useful for studying IRDCs is SiO, which traces shocked gas that could potentially be associated with energetic young outflows.

1.3 Formation of IRDCs

Molecular clouds are characterised by high turbulent pressures and are self-gravitating rather than in pressure equilibrium with other phases in the interstellar medium (Tielens 2010). Simulations have shown that the mechanisms that lead to the formation of IRDCs, and that

the compression they undergo during their lifetime, can initiate massive stars formation in these clouds (Heitsch et al. 2009; Hennebelle et al. 2008; Van Loo et al. 2007; 2014). Among several theories, IRDCs are believed to form through gravitational collapse (Heitsch & Hartmann 2008), i.e., when sufficiently dense and cold, the cloud starts to contract due to its own mass. Other theories suggest that the shock waves released by supernova remnants and/or HII regions can compress the surrounding material, form IRDCs and trigger star formation therein (Hennebelle et al. 2008). Finally, IRDCs have been proposed to form through cloud-cloud collisions of pre-existing GMCs, that produce a compressed layer between the clouds with a high enough column density for star formation to begin (Van Loo et al. 2007; 2014).

1.4 Aims and outline of the thesis

The main aim of this thesis is to examine the kinematic and physical conditions of the IRDC G28.23-0.19 and its massive cores − with the purpose of gaining a better understanding of the process of massive star formation. Using a mass surface density map for the IRDC, massive cores therein are identified. Following this, a multi-wavelength IR analysis are performed in order to study the relative evolutionary stage of the cores. Thereafter, the spectra for the $J = 1 \rightarrow 0$ rotational transition for the two CO isotopologues ^{13}CO and C^{18}O are extracted with the purpose of analysing the kinematic structure of the cores as well as the whole cloud.

Moreover, multiple physical quantities of the cloud and its cores are estimated. This includes the depletion factor, which quantifies the amount of CO freezing out onto grains of interstellar dust (Tan et al. 2014). A virial analysis is performed as well, with the purpose of studying the gravitational stability of the cloud (Kauffmann et al. 2013). By performing this analysis, conclusions regarding the evolutionary stage of the cores, and their potential to eventually form massive stars, can be drawn. Note that other molecular species than CO, as well as several other physical properties, are not analysed in this study. This is therefore a preliminary work in which only a certain number of quantities for this particular IRDC are investigated.

The outline of the thesis is as follows:

- In chapter 2, the process of identifying the massive cores using a mass surface density map are presented. This chapter also includes an analysis of potential emission at different infrared wavelengths for the identified cores.
- In chapter 3, the study of the kinematic structure of the IRDC and its cores are presented. This includes an examination of the line profiles of the obtained spectra for ^{13}CO(1−0) and C^{18}O(1−0) through multi-Gaussian analysis.
- In chapter 4, the analysis of the physical conditions of the IRDC are presented. An introduction to the relevant equations is included, followed by a compilation of the values obtained for column density, depletion factor and virial parameters toward the cloud and its cores.
- In chapter 5, the results from the earlier chapters are discussed in relation to the underlying theory, the different methods used and previous research. Areas of improvement and ideas for future studies are also discussed. Finally, general conclusions of the thesis are presented.

2

Massive cores in the IRDC G28.23-0.19

In this chapter, the presence of massive cores in the IRDC G28.23-0.19 are investigated along with their relative evolutionary stage. A massive core is believed to be the first stage of massive star formation, with masses in range of 1 to 100 $M_\odot$. Here, the map of the mass surface density obtained for the cloud is used to identify massive cores, which appears as over-densities within the map. Following this, potential emission at different infrared wavelengths in the cores are analysed, with the purpose of identifying their relative evolutionary stage.

2.1 Data set

The mass surface density map here investigated has been obtained using the method reported in Butler & Tan (2009). As described by the authors, a model of the IR cloud background was obtained and then used to infer the cloud visual extinction from Spitzer 8 µm images. This is finally converted in mass surface density of HeH^+, see also Kainulainen & Tan (2013). At 8 µm, the angular resolution of Spitzer is around $2''$. Furthermore, the pixel size of this data is around $0.6''$.

The cores were then compared to images from the Spitzer telescope taken at the wavelengths 4.5, 8 and 24 µm, and from the Herschel telescope at 70 µm, in order to estimate their relative evolutionary stages. This was done using Aladin Sky Atlas, a software applied to visualise astronomical images and databases (Bonnarel et al. 2000). The images at 4.5 µm and 8 µm were obtained as part of the GLIMPSE Spitzer Survey (Benjamin et al. 2003), while the 24 µm image was obtaines by the MIPSGAL Spitzer Survey (Carey et al. 2005). Finally, the image at 70 µm were obtained from the Herschel telescope (Magnelli et al. 2013).

2.2 Dendrogram analysis

Dendrogram is a form of diagram where a tree represents the hierarchical structure of the data it is applied to (Robitaille et al. 2016). It consists of the structures *branches*, which split into substructures, and *leaves*, which have no substructures. To implement the dendrogram structure, the *astrodendro* package in Python was used. This package uses an algorithm which finds local peaks in an image, which becomes leaves. Any pixel adjacent to a single leaf is integrated into the leaf. A pixel which is adjacent to several structures is a part of a branch with the structures in question as substructures. When this algorithm is applied to a mass surface density map, the leaves corresponds to massive cores since they are identified by local maximums in density.

The algorithm requires three parameters to be specified as follows (Robitaille et al. 2016):

- *min_value*: This corresponds to the minimum intensity to be considered significant. Consistent with previous works (Cheng et al. 2018; Liu et al. 2018), the value has been

set to 4× the noise of the map (see below).

- *min_delta*: This is the minimum difference in intensity between two structures to be considered independent. In order to avoid the effects of noise fluctuation, the value has been set to 1× the noise.

- *min_npix*: This is the minimum number of pixels required for a peak to be considered a real structure. This corresponds to the number of pixels contained in the beam of the telescope.

As stated above, the beam diameter is around $2''$ (Fazio et al. 2004). By taking the size of the beam divided by the area of a pixel, the minimum number of pixels were calculated to min_npix = 9. In order to calculate the noise, a root mean square (RMS) value was calculated of the data in the map below 15 % of max intensity, or 0.076 g/cm^2. The RMS value obtained from this was 0.046 g/cm^2. Since the RMS value only takes into account the statistical fluctuations of the image, it does not account for systematic errors that might be introduced when converting the 8 µm image into the mass surface density map. In this study, systematic errors to account for $\sim$ 25 % of the noise was assumed. The final noise in the map was then estimated to be $\sim$ 0.06 g/cm^2.

As shown in Figure 2.1, seven independent structures were identified from the dendrogram analysis. In Figure 2.1, the contour of each core, shown in different colours, is superimposed with the mass surface density map in grayscale. The properties of each of the seven identified cores are presented in Table 2.1. This includes the coordinates of the cores in the J2000 reference system, their mean mass surface density Σ, their area A and their mass M. Since the dendrogram analysys only provides the number of pixels within a core, the area was obtained by multiplying the number of pixels by the pixel area in cm^2. For this, a kinematic distance of 5.1 kpc to the source was assumed (Sanhueza et al. 2012). The mass could then be calculated according to

$$M = A_{\rm pix} N_{\rm pix} \Sigma, \tag{2.1}$$

where $A_{\rm pix}$ is the pixel area and $N_{\rm pix}$ is number of pixels in the core.

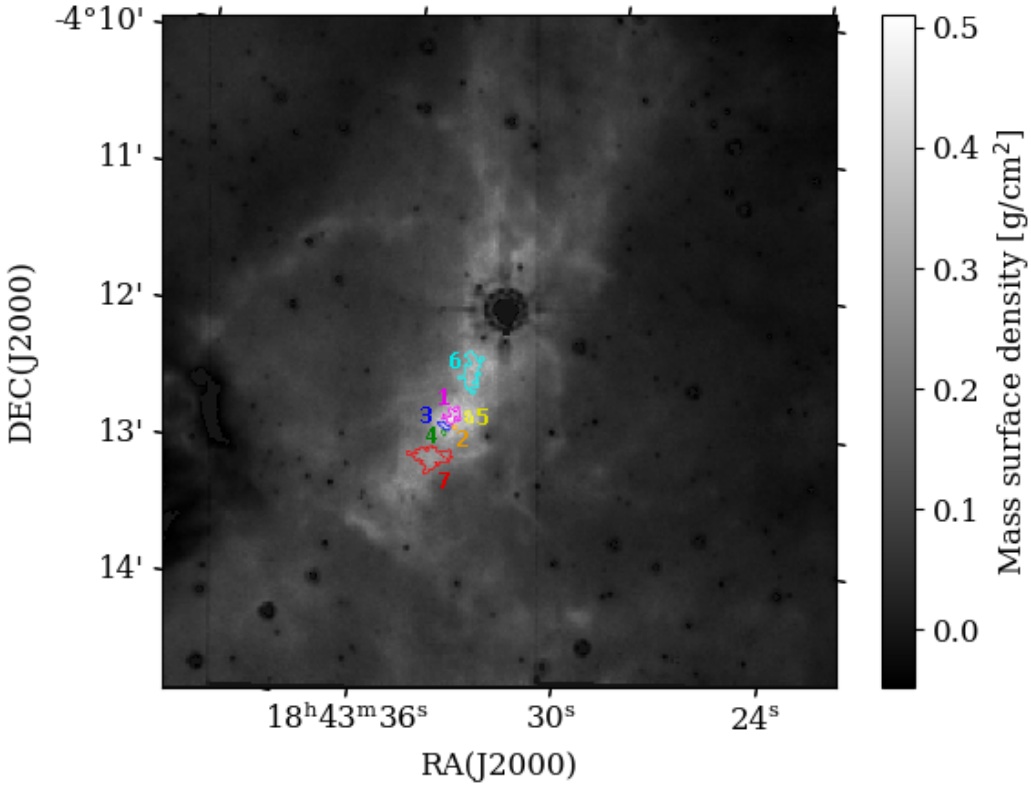

Figure 2.1: The contours of the leaves of the dendrogram, corresponding to the massive cores of the cloud, are shown in different colours. The contours of the cores are superimposed on the mass surface density map of the cloud, where the density in g/cm^2 is shown in grayscale.

Table 2.1: Properties of the identified cores. The second column indicates the colour shown in Figure 2.1. Moreover, the table includes the mean mass surface density Σ in g/cm^2, the area of each core in cm^2, and their mass in $M_\odot$. The coordinates for the cores are shown in the J2000 reference system.

Core	Colour	Right ascension (J2000)	Declination (J2000)	Σ [g cm^{-2}]	Area [cm^2]	Mass [$M_\odot$]
1	Purple	18:43:31.4	−04:13:17	0.4258	1.823×10^{35}	39.03
2	Orange	18:43:31.4	−04:13:22	0.4378	1.886×10^{34}	4.151
3	Blue	18:43:31.7	−04:13:21	0.4242	6.287×10^{34}	13.41
4	Green	18:43:31.7	−04:13:23	0.4186	2.096×10^{34}	4.410
5	Yellow	18:43:30.9	−04:13:19	0.4005	6.706×10^{34}	13.50
6	Cyan	18:43:30.6	−04:13:00	0.3256	5.407×10^{35}	88.49
7	Red	18:43:32.3	−04:13:33	0.2693	6.433×10^{35}	87.11

2.3 Infrared emission and evolutionary stages

In order to identify the level of star formation activity within each core, the presence of IR emission at multiple wavelengths was investigated. In particular, four main IR signatures of star formation were considered:

- 4.5 µm: This wavelength traces shock-excited emission from either H_2 or CO (Chambers et al. 2009). If that is the case, there are likely outflows due to star formation and the core could therefore be active.
- 8 µm: This wavelength traces polycyclic aromatic hydrocarbons (PAH) (Boquien et al. 2015; Hankins et al. 2020). PAH are formed as a byproduct of dust formation which can occur in dense molecular clouds (Peters 2002). However, Peeters et al. (2004) claims that even though PAH could be a convenient tracer of star formation, it is better suited to trace the formation of other forms of stars than massive ones.
- 24 µm: This wavelength traces warm dust at $\sim$ 100 K, due to thermal emission (Hankins et al. 2020), or very small grains of dust (Boquien et al. 2015). This could indicate embedded protostars as well as an active core (Chambers et al. 2009).
- 70 µm: Similarly to 24 µm, this wavelength traces thermal emission from dust, although colder dust at $\sim$ 40 K (Hankins et al. 2020). This wavelength could for example trace warm dust near embedded protostars (Giannetti et al. 2013).

The presence of one or more IR signature can be used to infer the relative evolutionary stages between the cores. In particular, according to the classification adopted by Chambers et al. (2009); a core is considered active if there are tracers for both 4.5 and 24 µm, quiescent if there are neither, and intermediate if one of the wavelengths are present but not the other. In Figure 2.2, the contours of the cores are presented together with each of the 4.5, 8, 24 and 70 µm images mentioned above.

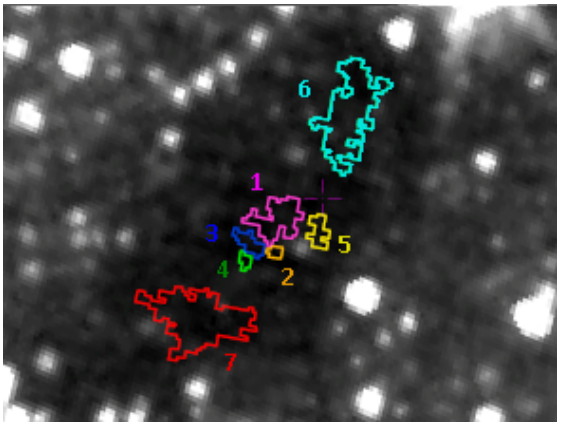

(a) 4.5 µm Spitzer image.

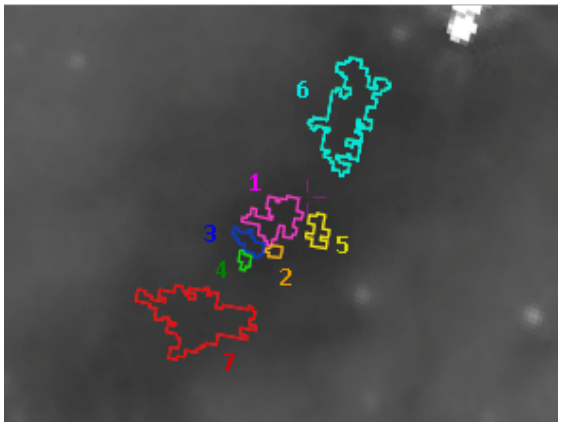

(b) 8 µm Spitzer image.

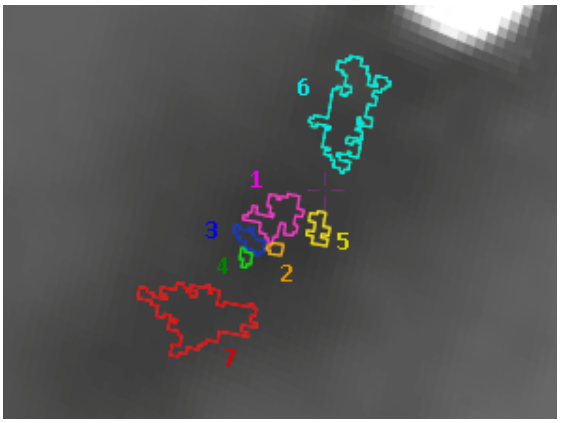

(c) 24 µm Spitzer image.

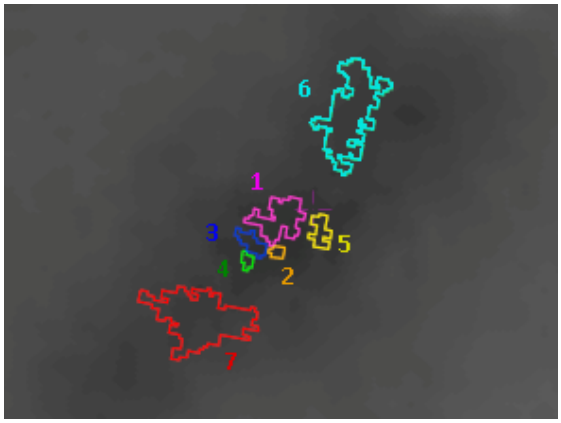

(d) 70 µm Herschel image.

Figure 2.2: The contours of the cores superimposed with maps at different wavelengths from the Spitzer (4.5, 8 and 24 µm) and Herschel (70 µm) telescopes. The colours of the cores correspond to those listed in Table 2.1.

The initial assessment is that since none of the cores overlaps with a source in any of the images, they can all likely be classified as quiescent. However, one point-like source for 4.5 µm could be observed near the clump of cores in the middle and could potentially be linked to one of the cores, the closest ones being core 1 and 5. As stated above, a presence of a 4.5 µm source could potentially indicate that the gas has been shocked, possibly due to outflow from star formation. Further implications of these results are discussed in greater depth in Section 5.1.

3

The kinematic structure of the IRDC G28.23-0.19

In this chapter, the kinematic conditions of the cloud are analysed. The kinematics of the molecular gas in and around IRDCs is deeply affected by the dynamical interaction of the cloud. On a smaller scale, the gas is highly processed by ongoing star formation activity. All this is reflected in the line profiles of multiple molecular tracers across IRDCs. The most abundant detectable at mm wavelengths molecule in IRDCs is CO. Here, the line profiles and kinematic structure of the CO isotopologue transitions ^{13}CO(1−0) and C^{18}O(1−0) are investigated at cloud and clump scale.

3.1 Data set

The CO emission data used in this study was collected from the FUGIN (FOREST Unbiased Galactic plane Imaging survey with the Nobeyama 45-m telescope) survey (Umemoto et al. 2017). The data is a 3D data set with two dimensions covering the cloud and the third being a velocity spectrum for each pixel. Furthermore, the line frequency is 115 GHz, the velocity resolution is 0.65 km/s, the angular resolution is 20.7″ and the spatial pixel resolution is 8.1″. The spectral noise, quantified by the RMS value, ranges between 0.09−0.60 K as seen in Table 3.3.

3.2 Kinematics of the cores

The kinematic conditions can be better understood by studying the shape (line profile) of the velocity spectra. If the spectra contain a single velocity peak with a Gaussian shape, the corresponding part of the cloud only has one velocity component. Multiple peaks, however, could potentially indicate the existence of multiple velocity components.

Due to the relatively low angular resolution of the CO emission data (20.7″, compared to 2″ for the mass surface density map), it was not possible to study the cores separately. Hence, three different regions across the cloud were selected, each with a radius of 10.35″ and containing one or multiple cores. From here on, these regions are referred to as “clumps”, a term commonly used for regions on a larger scale than cores (Sanhueza et al. 2012). The mass surface density map of the cloud is shown with the positions of the three selected clumps in Figure 3.1. Note that clump 1 contains core 6, clump 2 contains core 1−5 and clump 3 contains core 6. The coordinates for the centre of each clump in the J2000 reference frame are shown in Table 3.1.

In this section, the kinematics and line profile of these three clumps, as well as the cloud as a whole, are analysed. The spectra for the three clumps were extracted using SAOImageDS9 and can be seen in Figure 3.2.

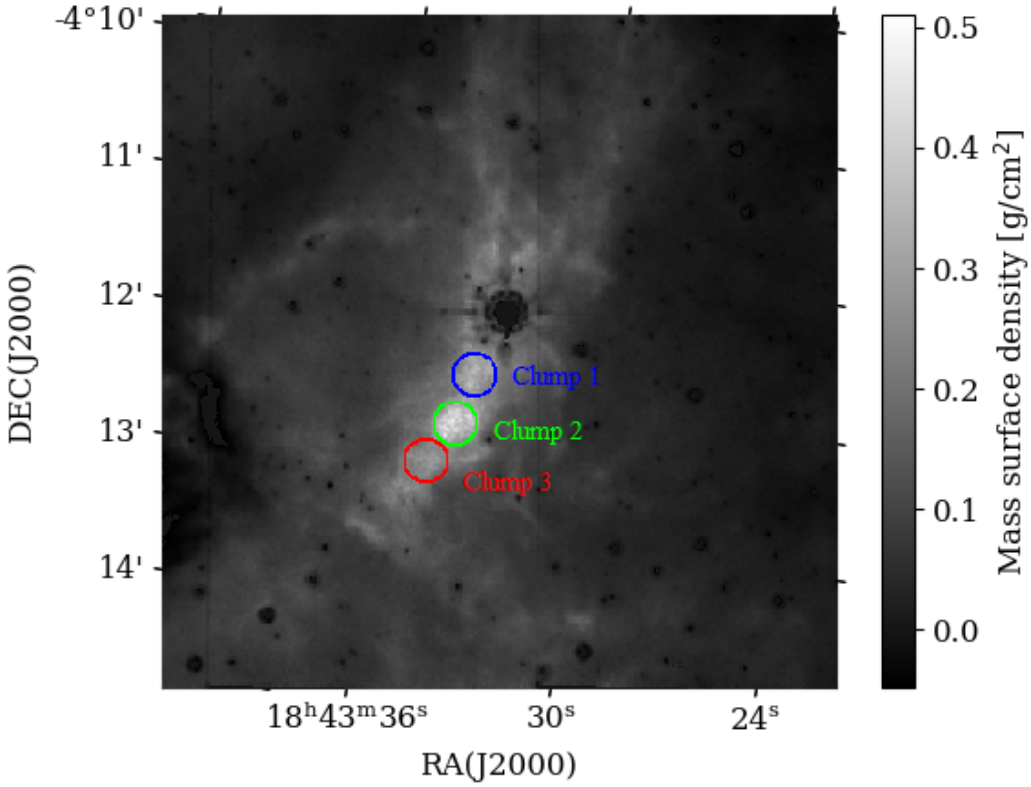

Figure 3.1: The three clumps, each with a radius of 10.35″, selected to include all of the identified massive cores can be observed here, superimposed on the mass surface density map. Clump 1 (blue) contains core 6, clump 2 (green) contains cores 1−5 and clump 3 (red) contains core 7. More information regarding the properties of the cores can be seen in Table 2.1.

Table 3.1: The table displays the colour and the coordinates (in the J2000 reference frame) for the clumps shown in Figure 3.1. The table also includes the corresponding cores.

Clump	Core(s)	Colour	Right ascension (J2000)	Declination (J2000)
1	6	Blue	18:43:30.4	−04:12:59
2	1−5	Green	18:43:31.3	−04:13:18
3	7	Red	18:43:32.4	−04:13:33

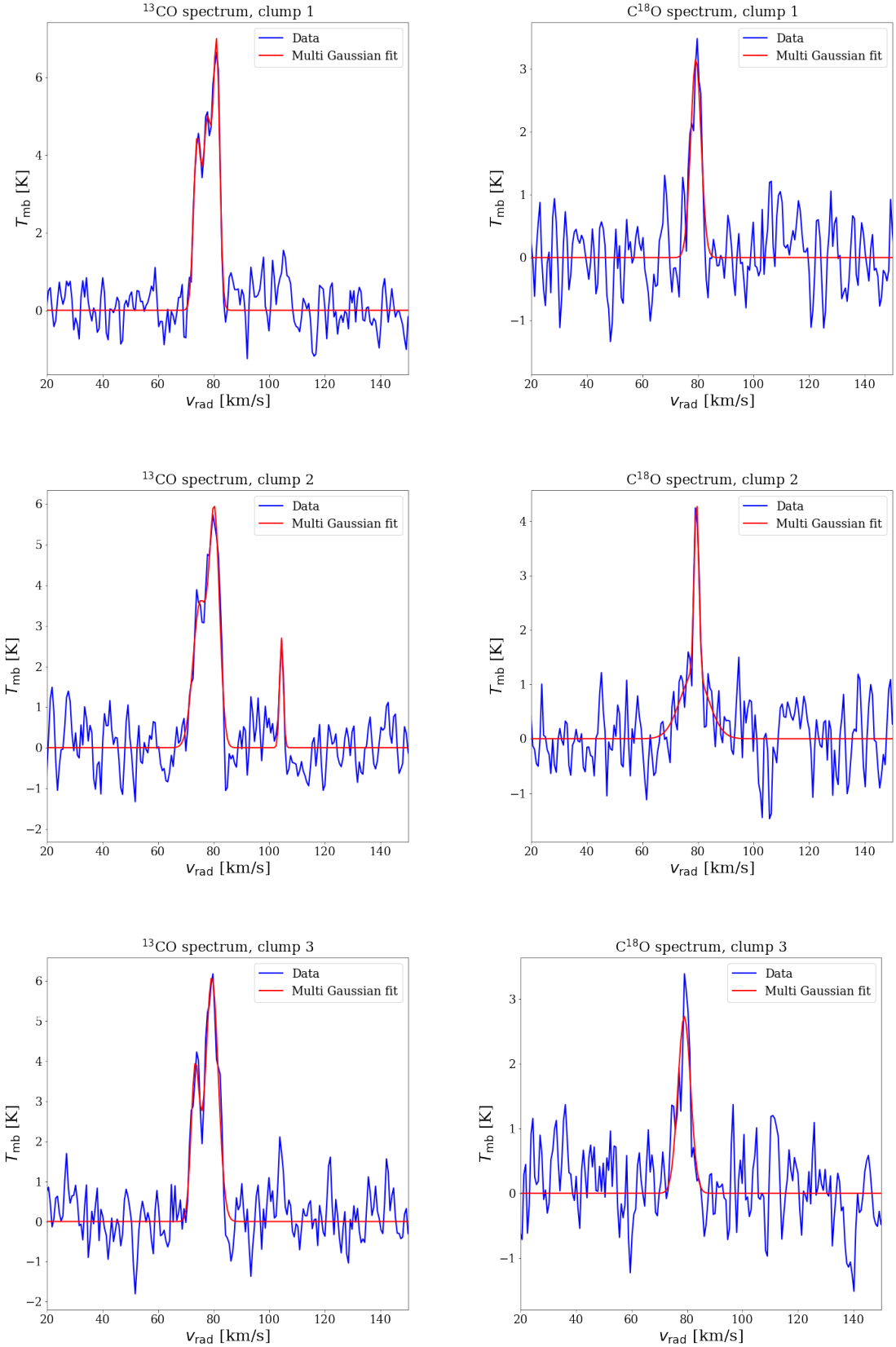

Figure 3.2: The ^{13}CO(1−0) and C^{18}O(1−0) spectra for the three clumps. The main beam brightness temperature T_{mb} in K is shown as the function of the radial velocity v_{rad} in km/s. The given isotopologue and clump are indicated on top of each panel.

From Figure 3.2, it can be noted that the line profile of the extracted spectra, in general, cannot be described by a single Gaussian since it shows some asymmetries. In particular, the presence of potential multiple velocity components, which is seen as multiple peaks in the spectra, can be observed.

As stated above, ^{13}CO and C^{18}O emits light of a certain frequency for the 1−0 transition. The emitted frequencies can be related to the velocities of the cloud with the Doppler effect (Simionato 2021; Vasyunina et al. 2011). The observed frequency f of a cloud moving towards the observer is higher relative to the emitted frequency f_0, whereas the case is reversed for a cloud moving away. The frequency can be related to the radial velocity according to

$$v_{\text{radial}} = c \cdot \frac{f_0 - f}{f_0}. \tag{3.1}$$

Multivariate Gaussian distribution models enabled the study of the velocity and line profile of the clumps. As shown in Figure 3.2 and Table 3.2, three velocity components for ^{13}CO were obtained toward clump 1 and clump 2, respectively. Two velocity peaks were observed for clump 3. The velocity dispersion, σ, of the multiple components was in the range 0.67−2.51 km/s for the three clumps. For the C^{18}O spectra, one velocity component toward clump 1, two toward clump 2 and one for clump 3 were observed. Here, the velocity dispersion of the multiple components was in the range 0.84−5.03 km/s for the three clumps.

To verify that the peak indeed corresponds to a velocity speak instead of noise, the area of the RMS of the spectra was compared to the area of the Gaussian fit of the peak. If the area of the Gaussian fit exceeded that of five times the RMS area, the peak could be considered real. For more details, see Appendix A.1. This was repeated for all peaks in each spectrum. To determine which Gaussian model that best fitted the data, χ^2 values were calculated for several models for each spectrum (Jeß 1989). The limit for when a model was considered good enough was a 15 % decrease in χ^2 when adding another Gaussian to the model. If the decrease in χ^2 was less than 15 %, the added Gaussian was deemed unnecessary. The RMS values and χ^2 values, for the ^{13}CO and C^{18}O spectra, of the Gaussian fits used are presented in Table 3.3. For more details on the calculations, see Appendix A.1.

Table 3.2: Values extracted from the Gaussian analysis. This includes the main beam brightness temperature T_{mb}, the peak velocity v, the velocity dispersion σ and the fraction $A_{\text{Gauss}}/A_{\text{RMS}}$, used to quantify the significance of the peaks. Note that properties for the spectra toward to whole cloud, analysed in Section 3.3, are included here as well.

	^{13}CO				C^{18}O			
Region	T_{mb} [K]	v [km s^{-1}]	σ [km s^{-1}]	$\frac{A_{\text{Gauss}}}{A_{\text{RMS}}}$	T_{mb} [K]	v [km s^{-1}]	σ [km s^{-1}]	$\frac{A_{\text{Gauss}}}{A_{\text{RMS}}}$
1	4.23	74.0	1.26	18.9	3.17	79.3	1.85	17.5
	4.88	77.8	1.55	24.2				
	6.47	81.1	1.13	27.3				
2	3.52	75.1	2.51	18.9	1.21	78.7	5.03	10.1
	5.57	80.3	1.82	25.4	3.21	79.5	0.84	11.0
	2.71	104	0.67	7.44				
3	3.78	73.4	1.48	15.0	2.74	79.0	2.28	15.0
	6.10	79.4	2.27	30.0				
Cloud	2.94	74.4	1.62	47.4	0.91	74.6	0.72	17.5
	4.45	79.9	2.41	87.6	1.13	79.7	2.39	39.3

Table 3.3: Error analysis for the Gaussian fits to the ^{13}CO and C^{18}O spectra. The table includes the estimated RMS noise the different spectra, as well as a χ^2 value used to estimate the quality of the fit. Note that properties for the spectra toward to whole cloud, analysed in Section 3.3, are included here as well.

	^{13}CO		C^{18}O	
Region	RMS [K]	χ^2-value	RMS [K]	χ^2-value
1	0.51	128.4	0.50	117.6
2	0.60	76.83	0.54	90.32
3	0.62	101.4	0.56	88.51
Cloud	0.16	177.2	0.09	90.30

Analysing the line profiles of the ^{13}CO and C^{18}O spectra for all three clumps of the IRDC G28.23-0.19 (see Figure 3.2), it can be noted that a single or multi (two or three components) Gaussian generally fit well with the obtained emission spectra. None of the line profiles of the different spectra show any clear broad wings, which indicates an absence of outflow activity in the cloud.

Furthermore, as seen in Figure 3.2, the ^{13}CO spectra indicates that all three clumps possibly have multiple velocity components. For the spectrum of clump 2, one peak stands apart with a higher velocity, around 104 km/s, than the larger part of the region. This could indicate that the clump contains portions of gas moving independently, or possibly that the peak corresponds to an object along the line of sight, unrelated to the clump. As seen in Figure 3.2, the C^{18}O spectra only shows one velocity component within each clump, the exception being clump 2 with two velocity components.

The velocity peaks in the C^{18}O spectra seems to mostly coincide with the most prominent peak in the spectra for ^{13}CO, see Table 3.2, where the highest difference between the two is 1.8 km/s. Additionally, the intensity and signal-to-noise-ratio of the C^{18}O spectra is lower than that of ^{13}CO. Since they might not be distinguishable from noise, this may be the reason for observing fewer velocity peaks in the C^{18}O spectra. The kinematic structure of the cores will be discussed further in Section 5.2.

3.3 Kinematics of the whole cloud

To investigate the kinematics of the whole cloud, a region with radius $100''$ covering the cloud, was selected (see Figure 3.3). As seen in Figure 3.4 and Table 3.2, two velocity peaks were obtained at 75 km/s and at 80 km/s. The velocity dispersion, σ, of the components was in the range $1.62-2.41$ km/s for ^{13}CO and in the range $0.72-2.39$ km/s for C^{18}O. Integrated intensity maps were obtained for the velocity peaks as seen in Figure 3.5.

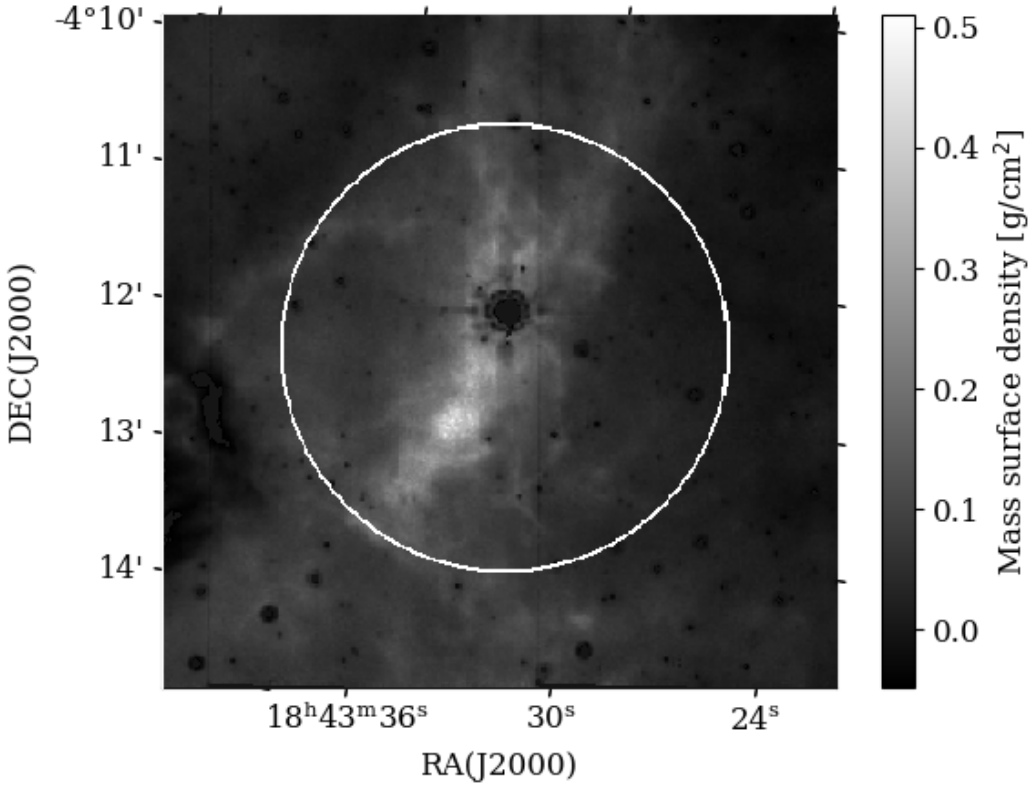

Figure 3.3: The region with radius 100″ selected for the study of the whole cloud, superimposed on the mass surface density map.

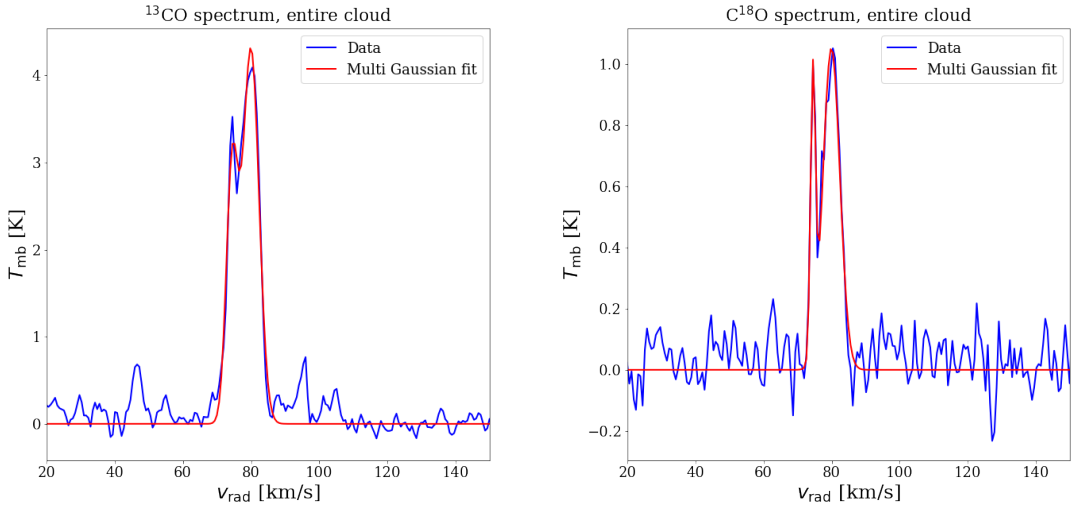

Figure 3.4: The ^{13}CO(1−0) and C^{18}O(1−0) spectra toward the whole cloud. The main beam brightness temperature $T_{\rm mb}$ in K is shown as the function of the radial velocity $v_{\rm rad}$ in km/s. The given isotopologue and are indicated on top of each panel.

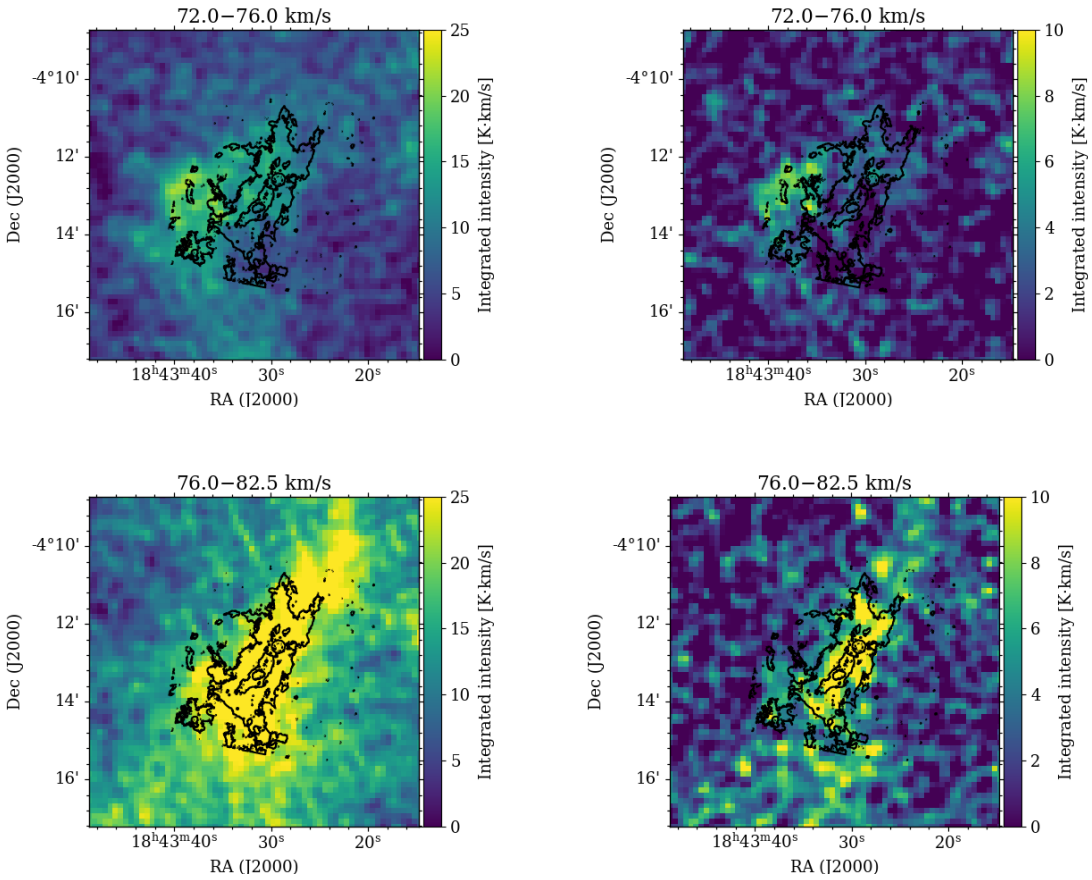

Figure 3.5: Integrated intensity maps for the velocity peak at 75 km/s and 80 km/s, respectively. ^{13}CO is shown to the right and C^{18}O is shown to the left. Contours from the mass surface density map of the cloud, superimposed on the intensity maps, are shown in black.

Analysing the line profiles of the ^{13}CO and C^{18}O spectra for the cloud as a whole in Figure 3.4, the same observation as for the clumps, regarding their Gaussian shapes, can be made. When observing the spectra for the whole cloud as well as the integrated intensity maps (see Figure 3.5), two velocity components can be found, one around 75 km/s and the other around 80 km/s, for both ^{13}CO and C^{18}O. When comparing the integrated intensity maps, it can once again be observed that C^{18}O has a lower intensity. Furthermore, the more prominent peak at 80 km/s is located at the centre of the cloud while the peak at 75 km/s seems to be located at the edge of the cloud for both ^{13}CO and C^{18}O. This could indicate that this velocity components is not part of the cloud, but rather an object along the line of sight. The kinematic structure of the cloud will be discussed further in Section 5.2.

4

Physical conditions of the IRDC G28.23-0.19

In this chapter, the analysis of physical conditions of the cloud are presented. In the first two sections, the quantities analysed are mainly column density and depletion factor for ^{13}CO and C^{18}O in the cloud. These quantities can provide information regarding the evolutionary stage of the cloud and the cores therein. In the third section, a virial analysis is performed where the virial parameter is estimated for all regions. From this quantity, conclusions regarding the gravitational stability of the cloud and its cores can be drawn. This could give an indication concerning their potential to form massive stars. Analogous to the kinematic analysis, the study in this chapter is performed for the three identified clumps as well as for the whole cloud.

4.1 Spectroscopic information

The analysis of the physical conditions in the cloud was performed for both ^{13}CO and C^{18}O. To enable this analysis, spectroscopic information regarding the rotational transition ($J = 1 \rightarrow 0$ in both cases) of the two isotoplogues were retrieved. This includes the rest frequency ν, the Einstein coefficient A, the rigid rotor rotation constant B_0 and isotopic ratio for the two CO isotopologues (^{12}C/^{13}C and ^{16}O/^{18}O for ^{13}CO and C^{18}O, respectively). All these quantities are reported in Table 4.1.

The values for the rest frequency and Einstein coefficient were retrieved from The Cologne Database for Molecular Spectroscopy (CDMS) (Müller et al. 2005). The values for the rigid rotor rotation constant B_0 were retrieved from studies by Cazzoli et al. (2003; 2004). The isotopic ratios were retrieved from the study by Wilson & Rood (1994).

Table 4.1: Physical quantities for the CO isotopologues studied. The table includes the rest frequency ν in GHz, the rotational transitions examined, the base 10 logarithm of the Einstein coefficient A, the rigid rotor rotation constant B_0 in GHz and the isotopic ratio. The isotopic ratio corresponds to ^{12}C/^{13}C and ^{16}O/^{18}O for ^{13}CO and C^{18}O, respectively.

Species	ν [GHz]	Transition	$\log_{10}(A)$ [$\log_{10}(\mathrm{s}^{-1})$]	B_0 [GHz]	Isotopic ratio
^{13}CO	110.201354	$J = 1 \rightarrow 0$	−7.49946	55.1010125	53
C^{18}O	109.782173	$J = 1 \rightarrow 0$	−7.20302	54.8914207	327

4.2 Column density

The molecular column density is a specific form of area density in which the volumetric density is integrated along a given path, or a "column" (Mangum & Shirley 2015). In astronomy, this quantity is generally used to estimate the number of molecules per area for

a given molecular species along the line of sight. The column density can be used to derive physical conditions of interest in the interstellar medium, such as the molecular abundance. Therefore, calculations of column densities from spectral lines are a fundamental part in the studies of molecular clouds.

If the medium studied is assumed to be uniform for a given excitation temperature $T_{\rm ex}$, the system have reached "local thermodynamic equilibrium", or LTE (Mangum & Shirley 2015). The excitation temperature corresponds to the expected temperature for a given system, with the two energy levels u and l, in which the number of particles in each state satisfies the Boltzmann equation. It is defined by the relation

$$\frac{n_{\rm u}}{n_{\rm l}} = \frac{g_{\rm u}}{g_{\rm l}} \exp\left(-\frac{\Delta E}{k_{\rm B} T_{\rm ex}}\right), \tag{4.1}$$

where ΔE represents the difference in energy between the two levels and $k_{\rm B}$ is the Boltzmann constant. Furthermore, $n_{\rm u}$ and $n_{\rm l}$ are the number of particles in the upper and lower state, respectively. Following the same notation, $g_{\rm u}$ and $g_{\rm l}$ correspond to the degeneracies for each level of a given transition. For a linear molecule, like CO, the total degeneracy for a rotational energy level J is calculated according to

$$g_{\rm J} = 2J + 1. \tag{4.2}$$

The total column density is obtained by relating the column density for one specific energy level to the entire population of all energy levels (Mangum & Shirley 2015). This is performed by applying the rotational partition function $Q_{\rm rot}$, which represents the relative population of the rotational energy levels for a given molecule. For a linear molecule, like CO, this is defined according to

$$Q_{\rm rot}(T) = \sum_{J=0}^{\infty} g_{\rm J} \exp\left(-\frac{E_{\rm J}}{k_B T}\right), \tag{4.3}$$

where g_J is defined according to Equation (4.2). If the rigid rotor approximation for the system is applied, and thus any centrifugal distortion is neglected, the energy levels E_J can be calculated according to

$$E_{\rm J} = hB_0 J(J+1), \tag{4.4}$$

where B_0 is the rigid rotor rotation constant. If the LTE conditions described earlier are assumed, the total column density for a molecular species can then be estimated according to

$$N = \frac{8\pi\nu^3}{Ac^3} \frac{Q_{\rm rot}(T_{\rm ex})}{g_{\rm u}} \frac{1}{J_\nu(T_{\rm ex}) - J_\nu(T_{\rm bg})} \frac{\exp(E_{\rm l}/k_{\rm B}T_{\rm ex})}{1 - \exp(-h\nu/k_{\rm B}T_{\rm ex})} \int T_{\rm mb} {\rm d}v. \tag{4.5}$$

Furthermore, this estimation assumes that the emission, studied in the molecular line spectrum, is optically thin (Vasyunina et al. 2011). This implies that no significant sources of attenuation are acting on the light emitted. Moreover, A is the Einstein coefficient, which describes the probability per unit time for spontaneous emission, i.e., that the system decays from a higher energy state to a lower one and emits a photon with corresponding energy. Furthermore, ν is the rest frequency for a given rotational transition, c is the speed of light and h is Planck's constant. $T_{\rm bg}$ is the cosmic microwave background temperature, which is approximately 2.73 K (Hernandez et al. 2011). $J_\nu(T)$ is the brightness temperature for a black body at temperature T. It is defined according to

$$J_\nu(T) = \frac{h\nu}{k_B} \frac{1}{\exp(h\nu/k_B T) - 1}. \tag{4.6}$$

This definition stems from Planck's law of black-body radiation, according to which the spectral radiance B from a black body can be calculated as

$$B_\nu(T) = \frac{2h\nu^3}{c^2} \frac{1}{\exp(h\nu/k_B T) - 1}. \tag{4.7}$$

The brightness temperature is therefore not a physical temperature, but rather an equivalent way to specify spectral radiance (Mangum & Shirley 2015). Note that E_l is the energy of the lower energy level, calculated according to this Equation (4.4). Lastly, T_mb is the main beam brightness temperature, which is integrated over a specific velocity interval for the given molecule.

The velocity intervals used here were 72−76 and 76−82.5 km/s, respectively. These intervals were chosen to correlate with the two observed peaks in most of the spectra, as described in Chapter 3. As stated in Section 3.3, the second interval most likely correspond to the overall kinematic structure of the cloud. For $C^{18}O$, the first peak was not observed for all regions. In these cases, this interval was left out. Furthermore, the integrated intensity was calculated for the whole interval 72−82.5 km/s in order to draw conclusions regarding the conditions of the total gas (while also excluding the noise outside of this interval). For the excitation temperature, a value of $T_\mathrm{ex} = 7.5$ K, with an error estimate of 20 %, was adopted based on the studies by Hernandez et al. (2011) and Hernandez & Tan (2015).

Moreover, it can be noted that $Q_\mathrm{rot}(T_\mathrm{ex})$ is defined as an infinite sum. For practical reasons, this was iterated until converging towards a sufficiently high value (3.19 for ^{13}CO and 3.21 for $C^{18}O$). Furthermore, the mass surface density Σ was estimated using the mass surface density map of the cloud. This was done by calculating an RMS value in Python from the pixels included in each of the regions, ignoring values below the estimated noise level 0.06 g/cm^2 (as described in Section 2.2).

Table 4.2 reports the column density in the different regions for ^{13}CO and $C^{18}O$, using $T_\mathrm{ex} = 7.5$ K. The table also reports the velocity interval with the corresponding integrated intensity, as well as the mass surface density of the different regions. Note that since no peaks could be observed in the interval 72−76 km/s for $C^{18}O$ in the clumps, likely due to its lower signal-to-noise-ratio, the column density was not calculated for this interval in these cases.

Figure 4.1 shows the column density as a function of excitation temperature for ^{13}CO and $C^{18}O$, respectively. Here the interval used is 76−82.5 km/s, as this most likely corresponded to the general kinematic structure in the cloud.

Table 4.2: Calculated column densities for ^{13}CO and C^{18}O, using $T_{\rm ex} = 7.5$ K. The table also includes the mean mass surface density Σ of each region, as well as the velocity intervals with corresponding integrated intensities.

Region	Σ [g cm^{-2}]	Interval [km s^{-1}]	$\int T_{\rm mb} {\rm d}v$ [K km s^{-1}]	$N(^{13}{\rm CO})$ [cm^{-2}]	$\int T_{\rm mb} {\rm d}v$ [K km s^{-1}]	$N({\rm C}^{18}{\rm O})$ [cm^{-2}]
1	0.293	72.0−82.5	46.3	8.99×10^{16}	14.9	1.46×10^{16}
		72.0−76.0	12.6	2.45×10^{16}		
		76.0−82.5	31.3	6.08×10^{16}	13.2	1.29×10^{16}
2	0.356	72.0−82.5	40.6	7.89×10^{16}	17.0	1.66×10^{16}
		72.0−76.0	10.6	2.05×10^{16}		
		76.0−82.5	28.1	5.45×10^{16}	13.3	1.30×10^{16}
3	0.245	72.0−82.5	40.9	7.95×10^{16}	15.2	1.48×10^{16}
		72.0−76.0	11.0	2.13×10^{16}		
		76.0−82.5	28.4	5.51×10^{16}	12.0	1.17×10^{16}
Cloud	0.136	72.0−82.5	33.8	6.56×10^{16}	7.98	7.78×10^{15}
		72.0−76.0	9.37	1.82×10^{16}	2.06	2.01×10^{15}
		76.0−82.5	22.5	4.38×10^{16}	5.58	5.44×10^{15}

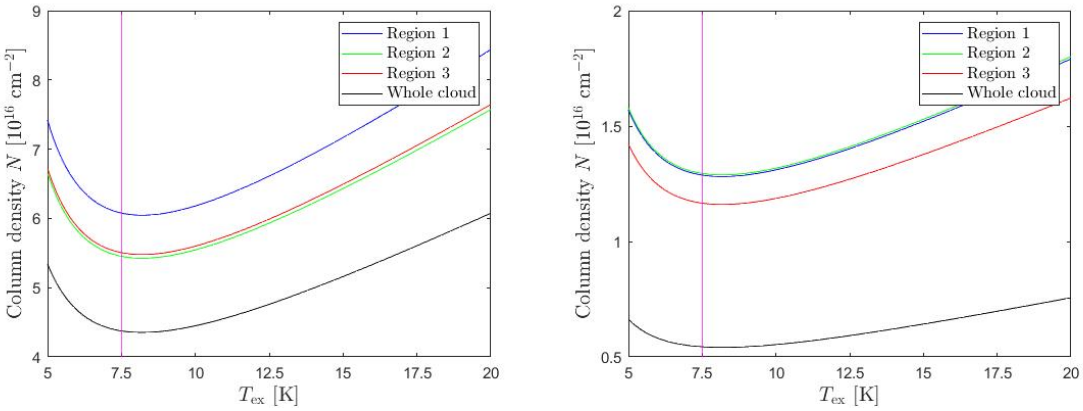

(a) Column density for ^{13}CO. **(b)** Column density for C^{18}O.

Figure 4.1: The column density N as a function of the excitation temperature $T_{\rm ex}$ for ^{13}CO and C^{18}O for the different regions. The vertical red line marks out $T_{\rm ex} = 7.5$ K, used in the calculations presented in Table 4.2. The velocity interval used is 76−82.5 km/s.

If Figure 4.1a is studied, it can be noted that the column density for ^{13}CO is highest for region 1 with a value at around 6.1×10^{16} cm^{-2} (for $T_{\rm ex} = 7.5$ K). Regions 2 and 3 show a lower value, around 5.5×10^{16} cm^{-2}, with the most dense region 2 being slightly lower. For C^{18}O, however, region 2 gives the highest value with around 1.3×10^{16} cm^{-2}, as seen in Figure 4.1b. The least dense region 3 gives the lowest values for the clumps with around 1.2×10^{16} cm^{-2}. For both isotopologues, the whole cloud gives the lowest column density. As seen in Table 4.2, these trends generally apply for the other velocity intervals as well. Further implications for these results are discussed in greater detail in Section 5.3.

As stated earlier, an excitation temperature of $T_{\rm ex} = 7.5$ K, with an error estimate of 20 %, was adopted. This would imply an excepted interval of $T_{\rm ex} = 6-9$ K. If Figures 4.1 are analysed, it can be seen that this at most results in an error of 6.5 % for both isotopologues. Moreover, it can be noted that the derivative ${\rm d}N/{\rm d}T_{\rm ex}$ is relatively low around 7.5 K.

Consequently, small changes in excitation temperature around this value does not affect the column density to a large degree. However, it is possible that the actual excitation temperature is outside of the assumed interval. Therefore, this error estimate might be on the low side. If the whole interval included in Figures 4.1 is considered (5−20 K), this could instead generate a maximum error for the column density in up to 40 %.

4.3 Depletion factor

As stated in Chapter 1, regions in molecular clouds with high potential to form stars are very cold and dense. As a consequence of these conditions, molecules normally found in gas phase can freeze-out onto grains of interstellar dust (Hernandez et al. 2011; Jiménez-Serra et al. 2014). This phenomenon is known as depletion. In a later evolutionary stage, the dust heats up and the CO molecules can return to gas phase. For CO, depletion is likely to occur for temperatures below 20 K (Tan et al. 2014). Since ^{13}CO traces slightly less dense gas than C^{18}O, ^{13}CO is likely to be more depleted in the dense cores (Danielson et al. 2013). The degree of depletion for a certain molecule is generally quantified by calculating the depletion factor $f_{\rm D}$. This quantity is defined as

$$f_{\rm D} = \frac{\chi(\text{species})_{\rm exp}}{\chi(\text{species})_{\rm obs}}, \tag{4.8}$$

where $\chi(\text{species})_{\rm obs}$ is the observed molecular abundance and $\chi(\text{species})_{\rm exp}$ is the excepted abundance, assuming standard gas phase abundances (Hernandez et al. 2011). The molecular abundance χ for a given species in a molecular cloud provides an indication on the occurrence of the species relative to the occurrence of H_2, which is the the most abundant molecule in the interstellar medium (Vasyunina et al. 2011). The abundance is determined according to

$$\chi(\text{species}) = \frac{N(\text{species})}{N(\text{H}_2)}, \tag{4.9}$$

where $N(\text{species})$ and $N(\text{H}_2)$ are the column densities for the molecular species in question and H_2, respectively. If different isotopologues of CO are analysed, as is the case in this study, the expected abundance can then be defined as

$$\chi(\text{species})_{\rm exp} = \frac{\chi(\text{CO})}{I}, \tag{4.10}$$

where $\chi(\text{species})$ is the molecular abundance of CO relative to H_2 and I is the ratio between the most abundant isotopologue ^{12}C^{16}O and the isotopologue in question (Hernandez et al. 2011; Jiménez-Serra et al. 2014). Using this definition, the column density of a given molecular species can be expressed as

$$N(\text{species}) = \Sigma(\text{species})\frac{1}{m(\text{H}_2)}\frac{\chi(\text{CO})}{I} = \Sigma(\text{species})\frac{\chi(\text{species})_{\rm exp}}{m(\text{H}_2)}, \tag{4.11}$$

where $\Sigma(\text{species})$ is the mass surface density of the species and $m(\text{H}_2)$ is the mass of a H_2 molecule. Similarly, the column density of H_2 can be estimated as

$$N(\text{H}_2) = \frac{\Sigma(\text{H}_2)}{m(\text{H}_2)}, \tag{4.12}$$

where $\Sigma(H_2)$ is the mass surface density of H_2 in region studied. Using Equation (4.9), the molecular abundance can consequently be expressed as

$$\chi(\text{species}) = \frac{N(\text{species})}{N(H_2)} = \frac{\Sigma(\text{species})}{\Sigma(H_2)}\chi(\text{species})_{\text{exp}}. \tag{4.13}$$

Thus, the depletion factor, according to its definition in Equation (4.8), can equivalently be calculated according to

$$f_D = \frac{\Sigma(H_2)}{\Sigma(\text{species})}. \tag{4.14}$$

To calculate the depletion factor, the column density for the isotopologues was converted into mass surfaces densities using Equation (4.11). Note that the abundance $\chi(CO) = 2 \times 10^{-4}$ was assumed (Jiménez-Serra et al. 2014). Regarding the isotopic ratios, see Table 4.1. For $\Sigma(H_2)$, the mass surface densities presented in Table 4.2 were assumed. Note that 2.34×10^{-24} g was assumed to be the mass per H nucleus (Hernandez et al. 2011; Jiménez-Serra et al. 2014). Thus, twice this value was assumed to be the mass for H_2.

Tables 4.3 and 4.4 presents the physical conditions for ^{13}CO and $C^{18}O$ described above. This includes the column density N and mass surface density Σ for the two isotopologues. The relation between these densities is given by Equation (4.11). Moreover, the velocity interval, the molecular abundance, the mass surface density for H_2 and the depletion factors are included.

Figure 4.2 shows the depletion factors calculated from the two isotopologues, the three velocity intervals and the four regions. Values for ^{13}CO and $C^{18}O$ are represented with a blue dot and red star, respectively. The velocity intervals are displayed in the same order as in Tables 4.3 and 4.4, i.e., 72−82.5, 72−76 and 76−82.5 km/s. Analogous to the column density, the depletion factor was not calculated for 72−76 km/s for the clumps in $C^{18}O$, since no peaks could be observed there. Regarding the regions, observe that the whole cloud is denoted as "C".

Table 4.3: Physical conditions for ^{13}CO. The table includes, from left to right, the velocity interval, the column density N, the molecular abundance χ relative to H_2, the mass surface densities Σ for ^{13}CO and H_2 and the depletion factor f_D.

Region	Interval [km s^{-1}]	$N(^{13}CO)$ [cm^{-2}]	$\chi(^{13}CO)$	$\Sigma(^{13}CO)$ [g cm^{-2}]	$\Sigma(H_2)$ [g cm^{-2}]	f_D
1	72.0−82.5	8.99×10^{16}	1.44×10^{-6}	0.112	0.293	2.63
	72.0−76.0	2.45×10^{16}	3.91×10^{-7}	0.030	0.293	9.66
	76.0−82.5	6.08×10^{16}	9.71×10^{-7}	0.075	0.293	3.89
2	72.0−82.5	7.89×10^{16}	1.04×10^{-6}	0.098	0.356	3.64
	72.0−76.0	2.05×10^{16}	2.69×10^{-7}	0.025	0.356	14.0
	76.0−82.5	5.45×10^{16}	7.17×10^{-7}	0.068	0.356	5.26
3	72.0−82.5	7.95×10^{16}	1.52×10^{-6}	0.099	0.245	2.49
	72.0−76.0	2.13×10^{16}	4.08×10^{-7}	0.027	0.245	9.25
	76.0−82.5	5.51×10^{16}	1.05×10^{-6}	0.068	0.245	3.59
Cloud	72.0−82.5	6.56×10^{16}	2.26×10^{-6}	0.081	0.136	1.67
	72.0−76.0	1.82×10^{16}	6.26×10^{-7}	0.023	0.136	6.03
	76.0−82.5	4.38×10^{16}	1.51×10^{-6}	0.054	0.136	2.51

Table 4.4: Physical conditions for $C^{18}O$. The table includes, from left to right, the velocity interval, the column density N, the molecular abundance χ relative to H_2, the mass surface densities Σ for $C^{18}O$ and H_2 and the depletion factor f_D.

Region	Interval [km s^{-1}]	$N(^{13}CO)$ [cm^{-2}]	$\chi(^{13}CO)$	$\Sigma(^{13}CO)$ [g cm^{-2}]	$\Sigma(H_2)$ [g cm^{-2}]	f_D
1	72.0−82.5	1.46×10^{16}	2.33×10^{-7}	0.112	0.293	2.63
	76.0−82.5	1.29×10^{16}	2.06×10^{-7}	0.099	0.293	2.97
2	72.0−82.5	1.66×10^{16}	2.18×10^{-7}	0.127	0.356	2.80
	76.0−82.5	1.30×10^{16}	1.70×10^{-7}	0.099	0.356	3.59
3	72.0−82.5	1.48×10^{16}	2.83×10^{-7}	0.113	0.245	2.16
	76.0−82.5	1.17×10^{16}	2.23×10^{-7}	0.089	0.245	2.75
Cloud	72.0−82.5	7.78×10^{15}	2.68×10^{-7}	0.060	0.136	2.28
	72.0−76.0	2.01×10^{15}	6.92×10^{-8}	0.015	0.136	8.84
	76.0−82.5	5.44×10^{15}	1.87×10^{-7}	0.042	0.136	3.27

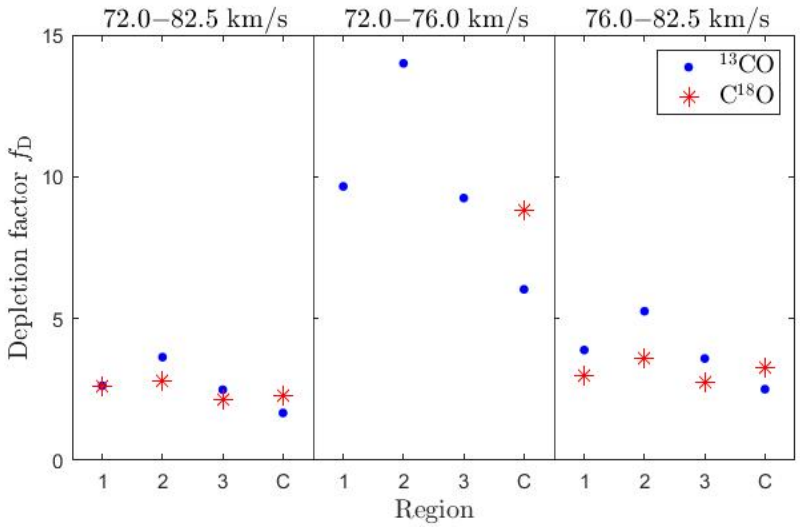

Figure 4.2: The depletion factor f_D for the different regions, velocity intervals and CO isotopologues. ^{13}CO is indicated with a blue dot and $C^{18}O$ is indicated with a red star. Note that the whole cloud is denoted as "C". Moreover, note that the depletion factor was not calculated for 72−76 km/s for the clumps in $C^{18}O$, since no velocity peaks could be observed there.

Studying Tables 4.3 and 4.4, as well as Figure 4.2, it can be noted that the gas moving with 76−82.5 km/s and 72−82.5 km/s showed depletion factors in the approximate ranges 2.5−5.3 and 1.7−3.6, respectively. The interval 72−76 km/s instead resulted in depletion factors around 6−14. Furthermore, it can be noted that the depletion factors toward the clumps is generally is a bit higher for ^{13}CO compared to $C^{18}O$. The difference in percentage ranges from 0−50 %. This, however, does not hold for the whole cloud, where the $C^{18}O$ depletion was higher with around 30−50 %.

When comparing the different regions, it can be noted that the dense (0.356 g/cm^2) region 2 generally seems to have a higher degree of depletion compared to the others. This is generally followed by region 2 (0.293 g/cm^2), region 3 (0.245 g/cm^2) and the whole cloud

(0.136 g/cm^2). The depletion therefore seems to increase with more dense regions. Further implications for these results, including sources of error, are discussed in greater detail in Section 5.3.

4.4 Virial analysis

In statistical mechanics, the virial theorem describes the relation between the average over time for the total kinetic energy and the potential energy in a system with multiple particles (Fedosin 2017; Kauffmann et al. 2013). The theorem states that

$$\langle T \rangle = -\frac{1}{2} \sum_{k=1}^{N} \left\langle \vec{F}_k \cdot \vec{r}_k \right\rangle, \tag{4.15}$$

where $\langle T \rangle$ is the average over time for the total kinetic energy, N is the number of particles and $\vec{F}_k$ is the force on the particle k in position $\vec{r}_k$.

In astronomy, the virial theorem can be used to estimate whether the gas in a molecular cloud is gravitationally bound or unbound (Kauffmann et al. 2013). In the first case, gravity is the dominant force affecting the particles in gas. This can lead to so-called "supercritical" fragments in the cloud, likely to undergo collapse and eventually form stars. In the latter case, the motion of the gas is instead affected by other forces, such as turbulence, in a larger extent. These "subcritical" fragments are more likely to expand and disperse into the interstellar medium. To analyse this in greater detail, the virial parameter $\alpha_{\rm vir}$ can be defined as

$$\alpha_{\rm vir} = \frac{5R\sigma^2}{GM}, \tag{4.16}$$

where R and M is the mean radius (given its size normal and along the axis of symmetry) and mass of the region, respectively. G is the gravitational constant and σ is the velocity dispersion of the gas. This definition stems from the observation that

$$\alpha_{\rm vir} = \frac{5R\sigma^2}{GM} = a\frac{2T}{|U|}, \tag{4.17}$$

where T and U are kinetic energy and potential energy for the gas, respectively. The parameter a accounts for geometrical effects of the region, such as non-spherical distributions of the density (Bertoldi & McKee 1992; Kauffmann et al. 2013). If a spherical region is assumed, $a = 1$. From this definition, it can be seen that low virial parameters correspond to a gravitationally bound state whereas a high value corresponds to gravitationally unbound state. The critical value between the states differs depending on the physical conditions of the region studied. For non-magnetized clouds, the threshold is around $\alpha_{\rm vir} \approx 2$ (Kauffmann et al. 2013).

The mass of the previously identified clumps, as well as the whole cloud, was estimated from the mass surface density map, by multiplying the mean mass surface density Σ for the assumed circular region with its physical area. Since circular regions with radius R were assumed, the mass could be calculated as $M = \Sigma\pi R^2$. The angular radius $R_{\rm a}$ was converted to physical scale by multiplying with the distance to the source $d = 5.1$ kpc (Sanhueza et al. 2012). Note that for the clumps, $R_{\rm a} = 10.35''$, and for the whole cloud $R_{\rm a} = 100''$ was assumed. Inserting the values for M and R in Equation (4.16), the virial parameter could

thus effectively be calculated as

$$\alpha_{\rm vir} = \frac{5\sigma^2}{G\Sigma\pi R_{\rm a} d} \tag{4.18}$$

Regarding the velocity dispersion σ, these were obtained by fitting one Gaussian to each of the spectra. Even though this, as seen in Chapter 3, is not the best approximation for most of the spectra, it was considered sufficient for this analysis.

An error estimate to the virial parameter, as well as the mass of each region, was calculated using the method of propagation of uncertainty, applied on Equation (4.18). To obtain an error estimate for the σ, confidence intervals generated in MATLAB, with a confidence level of 95 %m were used. For the mass surface density, a fixed value of ± 0.02 g/cm^2, based on the standard deviations for the densities within the regions. For the distance to the cloud, an error estimate of 10 % was used, based on the study by Sanhueza et al. (2017) about this cloud. Using the kinematic distance method and certain Galactic rotation curves, they obtained this error estimate by varying the velocity of the cloud with ± 5 km/s. For more details in error analysis, see appendix A.2.

Table 4.5 reports the results from the virial analysis, including the velocity dispersion σ and the virial parameter $\alpha_{\rm vir}$ for all different regions. As stated above, the errors estimates for σ and $\alpha_{\rm vir}$ were obtained using confidence intervals and propagation of uncertainty, respectively. Table 4.6 reports properties of the different regions, including their mass surface density, mass and radius. Furthermore, mean values for the viral parameter, with including error estimates, are included. Note that these error estimates were obtained by reapplying the propagating of uncertainty formula in Equation (A.3) to the mean value.

Figure 4.3 shows the virial parameter as a function of mass for the different clumps as well as the whole cloud. The critical value $\alpha_{\rm vir} = 2$, mentioned earlier, is marked out as a reference. The clumps are represented with a blue dot and the whole cloud with a red star.

Table 4.5: Results on the virial analysis for ^{13}CO and C^{18}O in the different regions. The table includes the velocity dispersions σ and virial parameters $\alpha_{\rm vir}$ with their respective error estimates.

	^{13}CO		C^{18}O	
Region	σ [km s^{-1}]	$\alpha_{\rm vir}$	σ [km s^{-1}]	$\alpha_{\rm vir}$
1	3.75 ± 0.32	14.5 ± 3.00	1.85 ± 0.36	3.53 ± 1.46
2	3.56 ± 0.40	10.7 ± 2.70	1.66 ± 0.32	2.33 ± 0.94
3	3.77 ± 0.42	17.5 ± 4.51	2.28 ± 0.52	6.43 ± 3.02
Cloud	3.84 ± 0.15	3.38 ± 0.66	3.40 ± 0.29	2.65 ± 0.65

Table 4.6: Physical properties of the different regions. The table displays the mass surface density Σ, the mass M, the angular radius R_{a}, the physical radius R and a mean value $\overline{\alpha_{\mathrm{vir}}}$ for the viral parameter.

Region	Σ [g cm^{-2}]	M [M$_\odot$]	R_{a} [$''$]	R [pc]	$\overline{\alpha_{\mathrm{vir}}}$
1	0.293	289 ± 61.0	10.35	0.26	9.00 ± 1.67
2	0.356	351 ± 72.9	10.35	0.26	6.54 ± 1.43
3	0.245	241 ± 52.1	10.35	0.26	12.0 ± 2.71
Cloud	0.136	$12\,500 \pm 3\,100$	100.0	2.47	3.02 ± 0.46

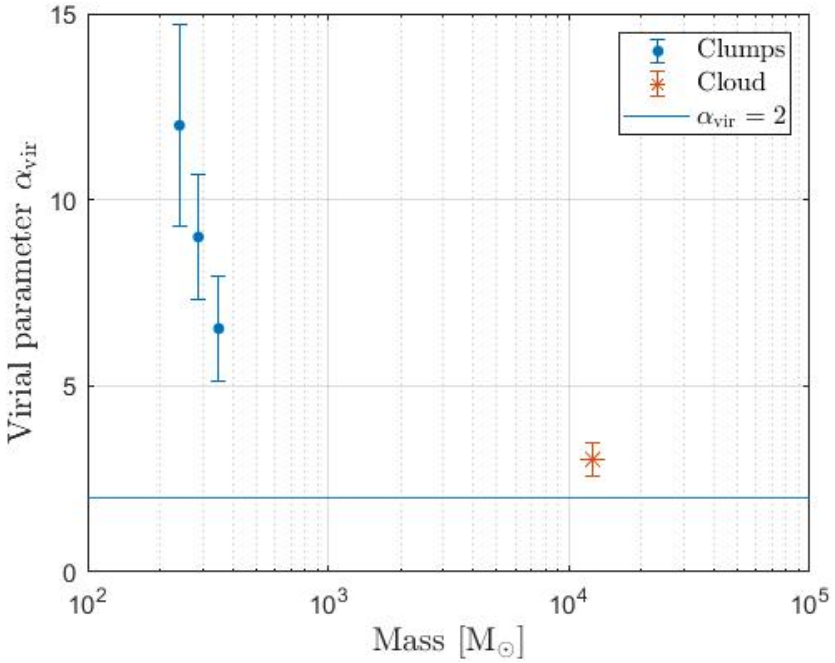

Figure 4.3: The virial parameter α_{vir} as function of the mass of the different clumps and the whole cloud. The critical value $\alpha_{\mathrm{vir}} = 2$ is marked out. The error estimates presented in Table 4.6 are indicated by error bars.

Analysing Tables 4.5 and 4.6, as well as Figure 4.3, it can be noted that all of the clumps show a mean virial parameter in the range 9−12. Since they all show $\alpha_{\mathrm{vir}} > 2$, this therefore indicates, by the virial theorem, that they are likely gravitationally unbound. The whole cloud shows a lower virial parameter, around $\alpha_{\mathrm{vir}} \approx 3$. Given its relatively low error margin, ± 0.46, it seems like the whole cloud could be gravitationally unbound as well.

In general, more massive regions tends to have a lower virial parameter and thus be more gravitationally bound. There are, however, multiple sources of error in the estimates made here. Therefore, these conclusions cannot be considered as rather certain. The sources of errors, and further implications for the results, are discussed in greater detail in Section 5.4.

5

Discussion

In this chapter, the results presented in earlier chapters are discussed in relation to the underlying theory, the different methods used and previous research. Furthermore, the consequences of the limitations of the study are discussed, as well as whether some of the assumptions made were reasonable. Additionally, areas of improvement and implications for future studies are also discussed. In the final section, general conclusions of the thesis are presented.

5.1 Massive cores and light emission

The process of using dendrogram to identify cores required some estimation of the parameters. As mentioned in Section 2.2, the noise used to create a dendrogram was approximately 30 % higher, i.e., 0.06 g/cm^2, than the noise calculated from the RMS value in order to compensate for systematic errors. However, it is difficult to obtain the exact amount of noise that stems from systematic errors. Consequently, there is a slight uncertainty in the value obtained.

Since cores 6 and 7 (corresponding to clumps 1 and 3, respectively) are both larger and less dense than the rest of the cores, it is possible that they are not cores at all, but rather just a disparity in the cloud density, such as extended substructures from the other cores. Considering that the leaf representing core 7 disappears if the value of the noise increases from 0.06 g/cm^2 to 0.065 g/cm^2, this region is specifically questionable. However, core 6 seems more robust since its leaf only disappeared upon increasing the value of the noise to 0.08 g/cm^2, which would also merge some of the cores in region 2.

A previous study on IRDCs by Rathborne et al. (2006) identified 3 cores in G28.23-0.19, whereof only one these cores coincide with the results obtained here. However, the study by Sanhueza et al. (2012), which uses the same data as Rathborne et al. (2006), refers to these cores as clumps. Considering the size of these objects, clumps would coincide more with the terminology used in this thesis. In that case, there are likely more than one core in this clump. Another study of G28.23-0.19 concluded that there are four cores residing in that region (Sanhueza et al. 2017). This paper also found another core, which seemed to coincide with the clump that Rathborne et al. (2006) found to not be associated with the IRDC.

The fact that five of the cores detected seemed to surround a source at 4.5 µm makes it seem like there could be emission at this wavelength around this region. If that is the case, it would mean that there could be intermediate cores and not only quiescent ones. This motivates that further investigation would be needed. However, Sanhueza et al. (2013) concluded that G28.23-0.19 is in a very early evolutionary stage due to lack of emission at 3.6, 4.5, 8.0, 24 and 70 µm wavelength, apart from an IR source coinciding with the northern part of the cloud. This IR source is a low-mass OH/IR star and since it is located in the foreground it was considered to not have any connection to our cloud. Therefore, it was excluded from this analysis. The finding by Sanhueza et al. (2013) would however coincide with the initial conclusions that the cores does not show emission at any of the wavelengths analysed. This

would consequently indicate the all of cores seem to be quiescent, or in an early evolutionary stage.

5.2 Kinematic structure

As seen in Figure 3.2 in Chapter 3, the line profiles of the ^{13}CO and C^{18}O spectra for all three clumps have a single Gaussian, or multi-Gaussian, shape. The same observation was made for the cloud as a whole, see Figure 3.4. Furthermore, none of the line profiles of the different spectra showed broad wings. This indicates an absence of outflow activity in the cloud, a conclusion supported by Tan (2018), Sanhueza et al. (2017) and Dirienzo et al. (2015) for the IRDC G28.23-0.19. The absence of outflow activity also supports the conclusion that G28.23-0.19 is currently star-less or in the stage of very early star formation (Sanhueza et al. 2017).

Additionally, the ^{13}CO spectra show multiple velocity components within each clump. Other studies agree that the IRDC show evidence of clumps and velocity substructure (Dirienzo et al. 2015; Liu et al. 2018). When considering the spectra of clump 2, the velocity peak at 104 km/s is most likely an object along the line of sight, unrelated to the clump. The C^{18}O spectra only show one velocity component for each clump, the exception being clump 2 with two velocity components. These velocity peaks seem to mostly coincide with the most prominent peak of the spectra for ^{13}CO, see Table 3.2. Furthermore, the reason for not observing the corresponding smaller velocity peaks in the C^{18}O spectra could be due to the lower signal-to-noise-ratio of the C^{18}O. Thus, these peaks cannot be distinguished from noise.

When observing the spectra for the whole cloud (see Figure 3.4) as well as the integrated intensity maps (see Figure 3.5), two velocity components were found around 75 km/s and 80 km/s for both ^{13}CO and C^{18}O. Furthermore, as seen in Figure 3.5, for both ^{13}CO and C^{18}O, the peak at 80 km/s is located at the centre of the cloud while the peak at 75 km/s is located at the edge of the cloud. As stated in Chapter 3, this likely indicates that the velocity component around 75 km/s is an object along the line of sight and unrelated to the cloud. This conclusion is also supported by other studies who have observed the velocity peak at 80 km/s (Dirienzo et al. 2015; Sanhueza et al. 2013), but do not mention one at 75 km/s. Therefore, the general kinematic structure of the cloud is likely represented with one mutual velocity component.

The absence of wing emission and outflow activity suggests that the cloud has not been formed via shock waves from supernovae. Furthermore, not much can be said about the other scenarios, gravitational collapse and cloud-cloud collisions, either. It could be argued that the two different velocity components indicate some form of collision, but as stated above it is more probable that one of them is unrelated to the cloud. Hence, no definite conclusions can be drawn regarding to the formation of IRDC G28.23-0.19 in this study. Therefore, further investigation is needed.

5.3 Column densities and depletion factors

In Section 4.2, the column densities for the different regions was estimated. As shown in the presentation of the results, region 1 gives the highest column density for ^{13}CO. For $T_{\mathrm{ex}} = 7.5$ K and the velocity interval $76-82.5$ km/s, shown in Figure 4.1, this value is

around 6.1×10^{16} cm^{-2}. For $C^{18}O$, the most dense region 2 gives the highest value with around 1.3×10^{16} cm^{-2}, whereas region 3, with the lowest density, gives the lowest value for the clumps. Given that $C^{18}O$ in general traces slightly more dense gas compared to ^{13}CO, this might be regarded as reasonable (Danielson et al. 2013). However, this does not hold for ^{13}CO where the least dense region 2 gives a lower column density than region 1. Furthermore, the whole cloud, which is less dense than its cores within, generates the lowest depletion factor for both isotopologues. This could be due to the several sources of errors discussed below.

Moreover, the depletion factor was calculated in Section 4.3 based on the column density calculations. From the results presented in Table 4.3, Table 4.4 and Figure 4.2, it can be noted that values around 1.7−5.3 was obtained for the velocity intervals 76−82.5 km/s and 72−82.5 km/s. For 72−76 km/s, higher values were obtained, ranging from 6 to 14. This might indicate that the gas moving at these velocities are more depleted, and thus colder, than the gas moving at 76−82.5 km/s, as well as the approximated total gas (72−82.5 km/s). However, this interval might not be the most suitable one for the cloud. As stated in section 5.2, the velocity peak roughly corresponding to this interval might not be a part of the cloud, but rather to material in the line of sight. Therefore, the depletion factors obtained for 76−82.5 km/s (2.5−5.3) might be regarded as representative for the cloud.

It can be noted that ^{13}CO, toward the different clumps, shows a higher depletion factor compared to $C^{18}O$ with up to 50 %. Consequently, this could be an indication that ^{13}CO are more depleted in these regions. As stated above, $C^{18}O$ is a tracer of denser gas compared to ^{13}CO. In dense regions, such as the cores, $C^{18}O$ would therefore be expected to be less depleted than ^{13}CO. This could potentially explain why $C^{18}O$ depletion is higher with 30−50 % when analysing the cloud as whole, which is less dense compared to its cores within. With regards to the theory, the results obtained could therefore be regarded as fairly reasonable. Furthermore, depletion seems to be higher for denser regions, with the dense region 2 resulting in the highest factors. This is excepted, given that CO is likely to freeze-out onto grains of dust in cold and dense regions (Hernandez et al. 2011; Jiménez-Serra et al. 2014).

As mentioned in Section 4.3, a high level of depletion towards a core could indicate an early evolutionary stage. Compared to other studies, both Hernandez et al. (2011) and Jiménez-Serra et al. (2014) studied CO depletion the IRDC G35.39-0.33, applying the same values for the expected abundances and isotopic ratios as here. By analysing $C^{18}O$ data for three different regions, Jiménez-Serra et al. (2014) found depletion factors in the range 5−12. They concluded that this were comparable to depletion factors found in massive starless cores. These results are also consistent to those of Fontani et al. (2012), who concluded that the earliest stages of massive star formation processes generally show depletion factors larger than those found in pre–stellar cores. As stated by Tan et al. (2014), there is, however, a big variety in depletion factors across IRDCs, where values up to 10^3 have been found.

The depletion factors obtained by Jiménez-Serra et al. (2014) are generally higher than most of the values estimated in this study. As stated earlier, the velocity interval 76−82.5 km/s most likely corresponds to the kinematic structure of the cloud. This interval resulted in depletion factors around 2.5−5.3. This could therefore potentially indicate that the cores in the cloud are in a later evolutionary stage. In such a stage, the cores increase in temperature, leading to CO returning to gas phase. This would, however, contradict the results discussed in Section 5.1, and especially not observing 24 µm or 70 µm emission, which traces warm dust. These results instead pointed towards the cores being in an earlier evolutionary

stage. However, as stated in Section 5.1, cores 6 and 7 might not be actual cores, given their comparatively lower densities ($\sim$ 0.3 g/cm^2) and higher masses ($\sim$ 90 $M_\odot$). Therefore, it is possible that the higher depletion factor around 5, found in region 2, is more representative. This could support the conclusion regarding the cores being quiescent or in an early evolutionary stage.

In the calculation for the column density and depletion factors, several assumptions were made, which implies potential sources of error. The formula used for calculating the total column density, Equation (4.5), assumed LTE conditions, as well as optically thin emission (Vasyunina et al. 2011). Since ^{13}CO and C^{18}O, unlike regular CO, is regarded as optically thin, this assumption could be seen as reasonable (Jiménez-Donaire et al. 2017). The LTE condition is harder to quantify, given the uncertainty in the excitation temperature. The study by Mangum & Shirley (2015) includes an analysis of column density estimations for non-LTE conditions. In new examinations, this could be examined in greater depth.

Furthermore, an excitation temperature of $T_{\text{ex}} = 7.5$ K with 20 % error margin, was assumed for both isotopologues, based on the work by Hernandez et al. (2011). This quantity is difficult the estimate and generates as error in the calculation for the column density. As discussed in Section 4.2, the assumed error lead to errors in the column density with up to 6.5 %. This might be on the low side, given the difficulties in measuring T_{ex}. For example, Du & Yang (2008) studied this IRDC and assumed a excitation temperature around $T_{\text{ex}} = 11.52$ K for both ^{13}CO and C^{18}O. Note that, since the calculation for the depletion factor is based on the column density calculation, the errors in excitation temperature (and other quantities) propagates to the depletion factor.

Furthermore, the depletion factor calculations assumed that the mass surface density Σ is an accurate measure for mass surface density $\Sigma(H_2)$. Therefore, other molecular species were neglected. However, since the abundance of other molecules is low compared to H_2, this could be considered as a reasonable estimate. Moreover, the choice of velocity intervals also affects the column density and depletion factor. The intervals used seemed to correlate with the peaks in most of the spectra, but the choice is a bit arbitrary and other limits generates slightly different values. This could also provide an explanation for the high depletion factors in the most narrow interval 72$-$76 km/s, given that the depletion factor is inversely proportional to the column density, and therefore to the integrated intensity.

In the calculation for the partition function Q_{rot}, the rotational energy level J were assumed to be $E_{\text{J}} = hB_0J(J+1)$. For a linear molecule like CO, a more accurate description of the energy levels would include higher order terms in the expansion of $J(J+1)$ in Equation (4.4) (Mangum & Shirley 2015). Thus, the centrifugal distortion constants were neglected here. For ^{13}CO and C^{18}O, the first two constants are around $D_0 \approx 170$ kHz and $H_0 \approx 0.15$ Hz (Cazzoli et al. 2003; 2004). Compared to B_0, this is in an order of 10^5 and 10^{11} smaller. Thus, the assumption to neglect these constants can be considered as reasonable.

5.4 Virial analysis

In Section 4.4, the virial parameter for the different clumps, as well as the whole cloud, was estimated. From the results presented in Table 4.5, Table 4.6 and Figure 4.3, it can be noted that the three different clumps all show a mean virial parameter $\alpha_{\text{vir}} > 2$. This implies that they are likely gravitationally unbound. Therefore, the turbulence motion of the gas in the cloud might be dominant compared to gravitational potential energy. When preformed for

the cloud as a whole, the analysis results in as smaller virial parameter. Therefore, the cloud seems to be more gravitational bound as a whole compared to the individual clumps. It still has, however, $\alpha_{\text{vir}} > 2$, indicating that the whole cloud is gravitationally unbound as well. This agrees well with studies suggesting that most molecular clouds tend to be unbound. According to Dobbs et al. (2011), this could potentially be due to cloud-cloud collisions, in which the energy input prevents gravitational forces to dominate.

Due to the insufficiency of kinetic energy, gravitationally bound cloud fragments are, if not balanced against self-gravity by significant magnetic fields, more likely become unstable (Kauffmann et al. 2013). Consequently, these fragments can undergo collapse and in time form massive stars. As stated, the cloud fragments studied here, given their virial parameters, seem to be unbound. This might indicate that these regions are not as likely to collapse and form stars. Studies by Larson (1981) show that $\alpha_{\text{vir}} > 2$ in fact dominates in many molecular clouds. This theory, known as "Larson's second law of cloud structure", indicates that star formation is a relatively slow process. The results here might therefore support this. On the other hand, other studies have discovered massive fragments in clouds where $\alpha_{\text{vir}} \ll 2$, which contradict this theory (Kauffmann et al. 2013).

The results obtained can also be analysed with the perspective of different types of star formation theories. According to the study by Kauffmann et al. (2013), one type of core accretion can occur when turbulent movement in the gas initially balances out self-gravity. This "turbulent core accretion" requires $\alpha_{\text{vir}} > 2$. On the other hand, competitive accretion is more likely to occur for low velocity dispersions and higher densities. Therefore, this phenomenon generally requires $\alpha_{\text{vir}} < 1$. This might indicate that cores studied here are more likely to undergo a turbulent core accretion. However, due to the multiple errors affecting these results, it is difficult to draw general conclusions regarding this.

Furthermore, the results obtained can be compared to studies about this particular IRDC. For example, the study by Dirienzo et al. (2015) analysed eight different clumps for this IRDC and found virial parameters in the range $0.8-3.5$. Moreover, the study by Sanhueza et al. (2017) analyses a specific massive clump with mass 1,500 $M_\odot$ and radius 0.6 pc. Given its coordinates, this clump roughly corresponds to region 1 and 2 (radius 0.2 pc each). According to Sanhueza et al. (2017), the virial parameter in this clump, and in the cores within, is approximately $\alpha_{\text{vir}} \approx 0.3$. Consequently, this would indicate that clump is gravitationally bound and likely to undergo collapse. Thus, this would indicate that this region could potentially form massive stars. This difference to the results obtained here might be due to how the velocity dispersion and mass surface density were obtained. For the cores studied, the study obtains a mean velocity dispersion 0.3 km/s, compared to $1.7-3.9$ km/s obtained here. This could potentially be due to higher velocity resolutions.

As mentioned above, there are several sources of error affecting these results. In Equation (4.18) used to calculate the virial parameter, there are errors in the estimations for the distance to the cloud d, the mass surface densities Σ and the velocity dispersions σ. As stated in Section 4.4, propagation of uncertainty was used to obtain an error estimate. The errors estimate for the different quantities might, however, not be entirely accurate. For example, errors in σ might be higher due to the choice of using the single Gaussian approximation. As this corresponded to the general velocity of the cloud, it was considered a sufficiently good model for this analysis. As stated by Kauffmann et al. (2013), this also avoids an arbitrary division of mass moving at different velocities. Additionally, the finite velocity resolution of 0.65 km/s introduces some uncertainty.

Furthermore, the virial analysis performed here does not take non-uniform density into account. This relates to the a parameter mentioned in Section 4.4. In new examinations, this could be studied in greater detail by analysing the density distribution of the cores. Finally, there are uncertainties regarding the mass estimates of the clumps and the whole cloud. According to Sanhueza et al. (2017), the mass of G28.23-0.19 is ~ 5000 $M_\odot$. The mass obtained from this study, 12,500 $\pm$ 3,100, is around 2.5 times bigger. For the whole cloud, an circular region with angular radius $100''$ were assumed. This choice is a bit arbitrary and might potentially explain the overestimate of the mass.

5.5 Future studies

This study was limited by the resolution of the telescopes used. The data obtained from FUGIN with the Nobeyama 45-m telescope only had an angular resolution of $20.7''$ (Umemoto et al. 2017). Therefore, cores 1−5 could not be observed individually, but had to be studied together as clumps. With more powerful telescopes, such as the Atacama Large Millimetre Array (ALMA) with a maximum resolution of $0.01''$, the cores could be studied individually (Baudry 2008). In future studies an increase in resolution, resulting in the study of the cores instead of larger clumps, might lead to a better understanding of the inner kinematics and physical conditions of this IRDC.

Moreover, a detailed analysis regarding noise reduction could also be performed. Vasyunina et al. (2011) applied an average spectra technique which enabled them to reduce the noise level and study weak emission lines. This could have been useful for the $C^{18}O$ analysis, given its low signal-no-noise-ratio. Furthermore, an analysis of the excitation conditions of the cloud could be performed in order to study the excitation temperature in greater detail. This would also enable the study of the column density without assuming LTE conditions, as described by Mangum & Shirley (2015).

To further study the kinematic and physical properties of the cloud, more examinations could be performed. Moreover, emission for several molecular species and their rotational transitions could be studied instead of relying solely on the emission from ^{13}CO and $C^{18}O$ at $J = 1 \rightarrow 0$. For example, as stated in Chapter 1, N_2H^+ is known to be a selective tracer of quiescent gas and is well suited for the study of the kinematic structure in cold cores (Vasyunina et al. 2011). Additionally, it allows a reliable measuring of the optical depth which was not studied here. Another molecular species mentioned in Chapter 1 that could be useful in further studies is SiO. This molecular species traces shocked gas, potentially associated with energetic young outflows (Bally 2016) and can reveal star formation activity for cores, even if there are no Spitzer sources apparent (Vasyunina et al. 2011).

Only a certain amount of physical quantities for CO in the cloud were analysed. For example, magnetic field properties were not considered. It is not fully understood how the collapse of massive cores is affected by magnetic fields, but it is widely accepted that the action of magnetic field and turbulence prevents fragmentation (Cosentino 2019). Therefore, the study of magnetic fields in relation to IRDCs could give an increased understanding of massive star formation.

5.6 Conclusions

In this thesis, the kinematic and physical conditions of the IRDC G28.23-0.19 and its massive cores have been examined. By analysing data from the mass surface density map of the cloud,

multi-wavelength infrared images, and emission spectra for $^{13}CO(1-0)$ and $C^{18}O(1-0)$, conclusions regarding the potential of the cloud to form stars can be drawn.

- The general lack of emission in the multi-wavelength IR analysis indicates that the cores within G28.23-0.19 likely are quiescent or in an early evolutionary stage. This agrees with the studies performed by Sanhueza et al. (2013; 2017). There were, however, some potential 4.5 µm emission towards cores in clump 2, most likely core 1 and 5. If this is the case, this could indicate shocked gas in this region and slightly more active cores.

- Regarding the kinematics of the cores and the cloud, there were signs of multiple velocity components within each region, generally around 75 km/s and 80 km/s. The velocity component around 75 km/s, however, seem to be unrelated to the cloud and most likely corresponds to material in the line of sight. Moreover, no indication of outflow activity in the cloud supports the conclusion that G28.23-0.19 is currently star-less or in the stage of very early star formation (Sanhueza et al. 2017).

- The depletion factors, calculated for the velocity most likely corresponding to the kinematic structure cloud (76−82.5 km/s), were in range 2.5−5.3. This is a slightly lower than depletion factors found in massive starless cores (Hernandez et al. 2011; Jiménez-Serra et al. 2014). Thus, this could potentially indicate warmer gas and therefore a later evolutionary stage, which contradicts the conclusions above. However, given the sources of error in the estimations, it is difficult to draw any certain conclusions.

- From the virial analysis performed, the cores seem to be gravitationally unbound with virial parameters spanning from 6.5 to 12. This could indicate that the cores are not likely to undergo competitive accretion. A more likely scenario could instead be "turbulent core accretion", in which turbulent movement in the gas initially balances out self-gravity. However, it is difficult to draw any general conclusions given the uncertainties of the method. For the different theories about IRDC formation, no definite and general conclusions can be drawn about the formation of G28.23-0.19 via shock waves from supernovae, gravitational collapse or cloud-cloud collisions.

In summary, this thesis has studied the kinematic and physical conditions of the IRDC G28.23-0.19 with the purpose of gaining a better understanding of the massive star formation process. Even though the cloud, in agreement with earlier studies, shows no clear indication of active star formation, it is worth noting that this thesis is a preliminary work in which only a certain amount properties and tracers of the gas in the cloud were analysed. It is therefore difficult to draw general conclusions regarding the formation of massive stars based on this examination alone. Consequently, further research is required in order to describe this IRDC, and its potential to form massive stars, in greater detail. However, this study has nevertheless provided some insight in the conditions for massive star formation, which future studies can build on.

Massive stars play an important role in the Universe, impacting the interstellar medium, as well as the evolution of galaxies and formation of planets (Tan et al. 2014). Through the study of infrared dark clouds, the believed birthplace of these massive stars, the process of massive star formation can be analysed. Consequently, studies of infrared dark clouds, like the one on G28.23-0.19 presented in this thesis, will continue to be of great interest in the field of astronomy.

References

Bally, J. 2016, ARA&A, 54, 491. doi:10.1146/annurev-astro-081915-023341

Baudry, A. 2008, 2nd MCCT-SKADS Training School. Radio Astronomy: Fundamentals and the New Instruments, 2-11

Battersby, C., Bally, J., Jackson, J. M., et al. 2010, ApJ, 721, 222. doi:10.1088/0004-637X/721/1/222

Benjamin, R. A., Churchwell, E., Babler, B. L., et al. 2003, PASP, 115, 953. doi:10.1086/376696

Bertoldi, F. & McKee, C. F. 1992, ApJ, 395, 140. doi:10.1086/171638

Bonnarel, F., Fernique, P., Bienaymé, O., et al. 2000, A&AS, 143, 33. doi:10.1051/aas:2000331

Boquien, M., Calzetti, D., Aalto, S., et al. 2015, A&A, 578, A8. doi:10.1051/0004-6361/201423518

Butler, M. J. & Tan, J. C. 2009, ApJ, 696, 484. doi:10.1088/0004-637X/696/1/484

Carey, S. J., Clark, F. O., Egan, M. P., et al. 1998, ApJ, 508, 721. doi:10.1086/306438

Carey, S. J., Noriega-Crespo, A., Price, S. D., et al. 2005, American Astronomical Society Meeting Abstracts

Cazzoli, G., Puzzarini, C., & Lapinov, A. V. 2003, ApJ, 592, L95. doi:10.1086/377527

Cazzoli, G., Puzzarini, C., & Lapinov, A. V. 2004, ApJ, 611, 615. doi:10.1086/421992

Chambers, E. T., Jackson, J. M., Rathborne, J. M., et al. 2009, ApJS, 181, 360. doi:10.1088/0067-0049/181/2/360

Cheng, Y., Tan, J. C., Liu, M., et al. 2018, ApJ, 853, 160. doi:10.3847/1538-4357/aaa3f1

Chira, R.-A., Beuther, H., Linz, H., et al. 2013, A&A, 552, A40. doi:10.1051/0004-6361/201219567

Cosentino, G. 2019, Ph.D. Thesis

Crapsi, A., Caselli, P., Walmsley, C. M., et al. 2005, ApJ, 619, 379. doi:10.1086/426472

Danielson, A. L. R., Swinbank, A. M., Smail, I., et al. 2013, MNRAS, 436, 2793. doi:10.1093/mnras/stt1775

Dirienzo, W. J., Brogan, C., Indebetouw, R., et al. 2015, AJ, 150, 159. doi:10.1088/0004-6256/150/5/159

Dobbs, C. L., Burkert, A., & Pringle, J. E. 2011, MNRAS, 413, 2935. doi:10.1111/j.1365-2966.2011.18371.x

Du, F. & Yang, J. 2008, ApJ, 686, 384. doi:10.1086/591221

Egan, M. P., Shipman, R. F., Price, S. D., et al. 1998, ApJ, 494, L199. doi:10.1086/311198

Fazio, G. G., Hora, J. L., Allen, L. E., et al. 2004, ApJS, 154, 10. doi:10.1086/422843

Fedosin, S. G. 2017, Continuum Mechanics and Thermodynamics, 29, 361. doi:10.1007/s00161-016-0536-8

Fontani, F., Giannetti, A., Beltrán, M. T., et al. 2012, MNRAS, 423, 2342. doi:10.1111/j.1365-2966.2012.21043.x

Giannetti, A., Brand, J., Sánchez-Monge, Á., et al. 2013, A&A, 556, A16. doi:10.1051/0004-6361/201321456

Hankins, M. J., Lau, R. M., Radomski, J. T., et al. 2020, ApJ, 894, 55. doi:10.3847/1538-4357/ab7c5d

Heitsch, F., Ballesteros-Paredes, J., & Hartmann, L. 2009, ApJ, 704, 1735. doi:10.1088/0004-637X/704/2/1735

Heitsch, F. & Hartmann, L. 2008, ApJ, 689, 290. doi:10.1086/592491

Hennebelle, P., Banerjee, R., Vázquez-Semadeni, E., et al. 2008, A&A, 486, L43. doi:10.1051/0004-6361:200810165

Hernandez, A. K., Tan, J. C., Caselli, P., et al. 2011, ApJ, 738, 11. doi:10.1088/0004-637X/738/1/11

Hernandez, A. K. & Tan, J. C. 2015, ApJ, 809, 154. doi:10.1088/0004-637X/809/2/154

Heyer, M. & Dame, T. M. 2015, ARA&A, 53, 583. doi:10.1146/annurev-astro-082214-122324

Jeans, J. H. 1928, Cambridge [Eng.] The University press, 1928.

Jeß, K. 1989, J. Quant. Spec. Radiat. Transf., 41, 69. doi:10.1016/0022-4073(89)90022-8

Jiménez-Donaire, M. J., Cormier, D., Bigiel, F., et al. 2017, ApJ, 836, L29. doi:10.3847/2041-8213/836/2/L29

Jiménez-Serra, I., Caselli, P., Fontani, F., et al. 2014, MNRAS, 439, 1996. doi:10.1093/mnras/stu078

Kainulainen, J. & Tan, J. C. 2013, A&A, 549, A53. doi:10.1051/0004-6361/201219526

Kauffmann, J., Pillai, T., & Goldsmith, P. F. 2013, ApJ, 779, 185. doi:10.1088/0004-637X/779/2/185

Krumholz, M. R. & Bonnell, I. A. 2009, Structure Formation in Astrophysics, 288

Larson, R. B. 1981, MNRAS, 194, 809. doi:10.1093/mnras/194.4.809

Liu, T., Kim, K.-T., Juvela, M., et al. 2018, ApJS, 234, 28. doi:10.3847/1538-4365/aaa3dd

Magnelli, B., Popesso, P., Berta, S., et al. 2013, A&A, 553, A132. doi:10.1051/0004-6361/201321371

Mangum, J. G. & Shirley, Y. L. 2015, PASP, 127, 266. doi:10.1086/680323

McKee, C. F. & Tan, J. C. 2003, ApJ, 585, 850. doi:10.1086/346149

Müller, H. S. P., Schlöder, F., Stutzki, J., et al. 2005, Journal of Molecular Structure, 742, 215. doi:10.1016/j.molstruc.2005.01.027

Perault, M., Omont, A., Simon, G., et al. 1996, A&A, 315, L165

Peeters, E., Spoon, H. W. W., & Tielens, A. G. G. M. 2004, ApJ, 613, 986. doi:10.1086/423237

Peters, W. 2002, Ph.D. Thesis

Pillai, T., Wyrowski, F., Menten, K. M., et al. 2006, A&A, 447, 929. doi:10.1051/0004-6361:20042145

Rathborne, J. M., Jackson, J. M., & Simon, R. 2006, ApJ, 641, 389. doi:10.1086/500423

Rathborne, J. M., Simon, R., & Jackson, J. M. 2007, ApJ, 662, 1082. doi:10.1086/513178

Robitaille, T., McDonald, B., Beaumont, C., & Rosolowsky, E. 2016, astrodendro Documentation: Release 0.3.0.dev. `https://dendrograms.readthedocs.io/_/downloads/en/latest/pdf/`

Sanhueza, P., Jackson, J. M., Foster, J. B., et al. 2012, ApJ, 756, 60. doi:10.1088/0004-637X/756/1/60

Sanhueza, P., Jackson, J. M., Foster, J. B., et al. 2013, ApJ, 773, 123. doi:10.1088/0004-637X/773/2/123

Sanhueza, P., Jackson, J. M., Zhang, Q., et al. 2017, ApJ, 841, 97. doi:10.3847/1538-4357/aa6ff8

Shu, F. H. 1977, ApJ, 214, 488. doi:10.1086/155274

Simionato, S. 2021, The Physics Teacher, 59, 333. doi:10.1119/10.0004881

Tan, J. C., Beltrán, M. T., Caselli, P., et al. 2014, Protostars and Planets VI, 149. doi:10.2458/azu_uapress_9780816531240-ch007

Tan, J. C. 2018, IAU Symposium, 332, 139. doi:10.1017/S1743921317009784

Taylor, J. 1997, Published by University Science Books, 648 Broadway, Suite 902, New York, NY 10012, 1997.

Tielens, A. G. G. M. 2010, The Physics and Chemistry of the Interstellar Medium, by A. G. G. M. Tielens, Cambridge, UK: Cambridge University Press, 2010

Umemoto, T., Minamidani, T., Kuno, N., et al. 2017, PASJ, 69, 78. doi:10.1093/pasj/psx061

Van Loo, S., Falle, S. A. E. G., Hartquist, T. W., et al. 2007, A&A, 471, 213. doi:10.1051/0004-6361:20077430

Van Loo, S., Keto, E., & Zhang, Q. 2014, ApJ, 789, 37. doi:10.1088/0004-637X/789/1/37

Vasyunina, T., Linz, H., Henning, T., et al. 2011, A&A, 527, A88. doi:10.1051/0004-6361/201014974

Wilson, T. L. & Rood, R. 1994, ARA&A, 32, 191. doi:10.1146/annurev.aa.32.090194.001203

A

Appendix 1

A.1 Gaussian error analysis

As stated in Chapter 3, it is important to quantify wheater a peak in an emission spectrum actually corresponds to a velocity speak instead of noise. This can be determined by calculating the area of the RMS noise in the spectrum. The result can then be compared to the area of the Gaussian fit of the peak. If the area of the Gaussian fit is larger than the RMS area by a certain factor (5 used here), the peak can be considered real. The area of the RMS was calculated according to

$$A_{\mathrm{RMS}} = \mathrm{RMS} \cdot \sqrt{\mathrm{FWHM} \cdot \mathrm{d}v}, \tag{A.1}$$

where $\mathrm{FWHM} = 2\sigma\sqrt{2\ln 2}$ corresponds to the full width at half maximum for the Gaussian fit, and $\mathrm{d}v$ is the velocity resolution of 0.65 km/s. To determine which Gaussian model that corresponds best to the data, the χ^2 test were applied to each spectrum. Here, the χ^2 was calculated according to

$$\chi^2 = \sum_{i=1}^{N} \frac{(y_{\mathrm{obs}} - y_{\mathrm{fit}})^2}{\mathrm{RMS}^2}, \tag{A.2}$$

where N is number of data points, y_{obs} is the observed value, y_{fit} is the value according to the fit and RMS corresponds to the estimated RMS noise (Jeß 1989). The model with the lowest χ^2 value is generally the best model. However, a model containing more Gaussians will always generate a lower value. Therefore, it is important to consider the relative decrease in the χ^2 value when adding Gaussians to the model. If the relative change in χ^2 is deemed small enough, the fit could be considered as sufficient.

A.2 Propagation of uncertainty

To estimate the error in the virial parameter, calculated according to Equation (4.18), propagation of uncertainty was used. For a function $X(\xi_1, , , \xi_n)$, this results in

$$X = X_0 \pm \delta X = X_0 \pm \sqrt{\sum_{i=1}^{n} \left(\frac{\partial X}{\partial \xi_i}\right)^2 (\delta\xi_i)^2}, \tag{A.3}$$

where δX and $\delta\xi_i$ is the error for the X and each of the variables, respectively, and X_0 is a particular value of X (Taylor 1997). Note that the derivative is evaluated at a particular value ξ_{i_0} and that correlations between the variables are neglected. Applied to the virial parameter and Equation (4.18), the results in

$$\delta\alpha = \alpha_0 \sqrt{\left(\frac{2\delta\sigma}{\sigma_0}\right)^2 + \left(\frac{\delta\Sigma}{\Sigma_0}\right)^2 + \left(\frac{\delta d}{d_0}\right)^2}. \tag{A.4}$$

Observe that this assumes that the only errors propagating to α_{vir} arise from the velocity dispersion σ of the gas, the mass surface density Σ of the region and the distance d to the cloud.